The Journal of Chemical Physics

RESEARCH ARTICLE | MAY 08 2024

Non-adiabatic excited-state time-dependent *GW* molecular dynamics (TD*GW*) satisfying extended Koopmans' theorem: An accurate description of methane photolysis

Aaditya Manjanath ; Ryoji Sahara ; Kaoru Ohno ; Yoshiyuki Kawazoe

J. Chem. Phys. 160, 184102 (2024)
https://doi.org/10.1063/5.0202590

AIP Publishing

The Journal of Chemical Physics ARTICLE pubs.aip.org/aip/jcp

Non-adiabatic excited-state time-dependent *GW* molecular dynamics (TD*GW*) satisfying extended Koopmans' theorem: An accurate description of methane photolysis

Cite as: J. Chem. Phys. 160, 184102 (2024); doi: 10.1063/5.0202590
Submitted: 5 February 2024 • Accepted: 22 April 2024 •
Published Online: 8 May 2024

Aaditya Manjanath,[1,a)] Ryoji Sahara,[1] Kaoru Ohno,[1,2] and Yoshiyuki Kawazoe[3,4,5]

AFFILIATIONS

[1] Research Center for Structural Materials, National Institute for Materials Science, 1-2-1 Sengen, Tsukuba, Ibaraki 305-0047, Japan
[2] Department of Physics, Yokohama National University, 79-5 Tokiwadai, Hodogaya-ku, Yokohama, Kanagawa 240-8501, Japan
[3] New Industry Creation Hatchery Center, Tohoku University, 6-6-4 Aramaki Aza Aoba, Aoba-ku, Sendai, Miyagi 980-8579, Japan
[4] School of Physics, Institute of Science, Suranaree University of Technology, 111 University Avenue, Nakhon Ratchasima 30000, Thailand
[5] Physics and Nanotechnology, SRM Institute of Science and Technology, Kattankurathur, Tamil Nadu 603203, India

[a)] **Author to whom correspondence should be addressed:** manjanath.aaditya@nims.go.jp

ABSTRACT

There is a longstanding difficulty that time-dependent density functional theory relying on adiabatic local density approximation is not applicable to the electron dynamics, for example, for an initially excited state, such as in photochemical reactions. To overcome this, we develop non-adiabatic excited-state time-dependent *GW* molecular dynamics (TD*GW*) on the basis of the extended quasiparticle theory. Replacing Kohn–Sham orbitals/energies with *correlated, interacting* quasiparticle orbitals/energies allows the full correspondence to the excited-state surfaces and corresponding total energies, with satisfying extended Koopmans' theorem. We demonstrate the power of TD*GW* using methane photolysis, $CH_4 \rightarrow CH_3^{\bullet} + H$, an important initiation reaction for combustion/pyrolysis and hydrogen production of methane. We successfully explore several possible pathways and show how this reaction dynamics is captured accurately through simultaneously time-tracing all quasiparticle levels. TD*GW* scales as $\mathcal{O}(N_B^{3-4})$, where N_B is the number of basis functions, which is distinctly advantageous to performing dynamics using configuration interaction and coupled cluster methods.

INTRODUCTION

Density functional theory (DFT)[1] together with local density approximation (LDA)[2] provides an excellent basis for the electronic structure calculations of materials. Since DFT is a ground state theory,[1] it obviously cannot be applied to excited states (ESs). Its time-dependent (TD) extension, TDDFT[3] or TDDFT molecular dynamics (TDDFT-MD), has been used to study ES dynamics. However, ES dynamics simulations[4–13] with TDDFT have inevitably relied on adiabatic local density approximation (ALDA),[14] which is valid only for the initial state being the ground state and not for any initially excited state, such as in photochemical reactions. *The applicability of ALDA to the electronic excitation caused by an applied field, even if starting from the ground state, is also questionable.* The lack of knowledge on the exact form of the exchange–correlation (xc) kernel applicable to any ES in TDDFT-MD has hampered any accurate and reliable theoretical investigation of the ES dynamics.[5] Another problem of LDA is that the energy of each one-electron level does not reflect the total energy of the corresponding Born–Oppenheimer (BO) surface.[2] This is because extended Koopmans' theorem[15,16] does not hold in DFT, although Janak's theorem[17] does. Therefore, when 2 one-electron levels cross each other during the dynamics simulation, the BO surfaces do not cross. This is related to the fact that energy gaps are severely

underestimated in LDA. Attempts to solve the bandgap underestimation problem have been made by using parametric hybrid functionals,[18] optimally tuned range-separated hybrid functionals,[19] localized orbital scaling correction,[20] as well as Koopmans-compliant functionals.[21] However, even with those functionals, the initially excited states cannot be handled.

A possible breakthrough has been achieved in this regard via the extended quasiparticle (QP) theory (EQPT),[22,23] which fully guarantees the applicability of Green's function method in the many-body perturbation theory (MBPT)[24] to any initially excited eigenstate of the Hamiltonian. Hence, the time-dependent quasiparticle (TDQP) equation can be applied to any system that starts from an arbitrary excited eigenstate. The extension of the TDQP equation to wavepackets for dynamics is straightforward under EQPT by defining a wavepacket to be a mixed state of QP wavefunctions. As a result, EQPT provides a firm basis to treat excited-state dynamics. The validity of EQPT has been demonstrated by the authors' (KO's) group[25–27] mainly by using the *GW* approximation (*GW*A).[28] *GW*A under EQPT guarantees that the *GW* QP energies are directly related to the total energies of the excited N and $(N \pm 1)$electron states, with extended Koopmans' theorem being satisfied.

In this work, this EQPT approach is extended to the non-adiabatic (NA) dynamics framework, which we name non-adiabatic excited-state time-dependent *GW* molecular dynamics, NA-ES-TD*GW*-MD or TD*GW* (see METHODS). The present work is an NA extension of the method used in the previous work[29] (however, no explanation and validation of EQPT was provided there), where the ES dynamics of the $CO^* + H \rightarrow HCO$ reaction was simulated. As a step toward NA simulations, trajectory surface-hopping,[30,31] full multiple spawning,[32,33] *ab initio* multiple spawning,[34,35] and *ab initio* multiple cloning[36] have been proposed.[37] Our formulation obeys an *ab initio* surface-hopping–like cloning technique, where the Ehrenfest mean-field trajectory with a hop to the BO surface is considered. Here, we use the TD Hartree approximation[38] for nuclei with delta-function–like orbitals, which enables us to treat electron wavepackets as a function of the mean values of the nuclear coordinates.

We choose methane photolysis to demonstrate the ability of NA-ES-TD*GW*-MD in correctly capturing the reaction dynamics. The applications of methane in heat production and in hydrogen generation are governed by its decomposition process in the ES. The voluminous literature on methane decomposition (irrespective of the method employed) clearly suggests that it is a complex multi-step process with the initiation reaction being $CH_4 \rightarrow CH_3^\bullet + H$.[39–55] Understanding the mechanism of this particular dissociation reaction is useful for predicting the details of subsequent reactions that eventually lead to the production of hydrogen.

Photolysis of methane has been explored extensively using both experimental[46–53] and computational[44–46] means. Computationally, TDDFT-MD has been applied to study (a) ionization of methane with a successive emission of hydrogen under a strong laser field,[10] (b) dynamics of ion–molecule interactions using $CH_4 + H^+$ as an example,[11,56] and (c) combustion of methane[12] by colliding O_2 with CH_4 at low collision energies of 6–10 eV. However, as mentioned previously, the applicability of the LDA xc functional to ESs is questionable.[5] An exception to these reports is the complete-active-space self-consistent field (CASSCF) study on the successive photolysis of methane by Lodriguito *et al.*;[57] however, their results are not very clear because no information is provided on the time evolution of natural orbitals, related occupation numbers, or quantities that can indicate the possibility of a successful dissociation. In the present work, we use the TD*GW* method to simulate methane photolysis through several pathways.

METHODS

A brief description of the extended quasiparticle theory (EQPT)

The most important advantage of EQPT is that the initial state need not necessarily refer to the ground state but can be an arbitrary excited eigenstate.[22,23] This is contrary to conventional wisdom that the reference state is always the ground state. In EQPT, the quasiparticle (QP) energy $\varepsilon_\lambda^{\rm QP}$ satisfies extended Koopmans' theorem[15,16] exactly and corresponds to the total energy difference between the N electron initial (or reference) state and the $(N \pm 1)$ electron final state. For example, the QP energy of an occupied orbital i, i.e., $\varepsilon_i^{\rm QP}$ is given by (see Fig. 1 and Appendix B)

$$\varepsilon_i^{\rm QP} = E_{\rm ref}^{(N)} - E_{i\rightarrow{\rm vac}}^{(N-1)}, \tag{1}$$

where $E_{\rm ref}^{(N)}$ and $E_{i\rightarrow{\rm vac}}^{(N-1)}$ are the true *GW* total energies of the reference N electron system and the $(N-1)$ electron system formed by removing an electron from the ith occupied level to the vacuum level (vac). The QP energy of an unoccupied level a, i.e., $\varepsilon_a^{\rm QP}$ can similarly be defined as [see Figs. 1(a) and 1(b) as well as Appendix B]

$$\varepsilon_a^{\rm QP} = E_{{\rm vac}\rightarrow a}^{(N+1)} - E_{\rm ref}^{(N)}, \tag{2}$$

where an electron is added from vac to the ath unoccupied level. At the point where a crossing between the ith and ath QP levels is encountered, the relation,

$$\varepsilon_a^{\rm QP} = E_{{\rm vac}\rightarrow a}^{(N+1)} - E_{\rm ref}^{(N)} = E_{\rm ref}^{(N)} - E_{i\rightarrow{\rm vac}}^{(N-1)} = \varepsilon_i^{\rm QP}$$

or

$$\Delta\varepsilon_{\rm gap} = E_{{\rm vac}\rightarrow a}^{(N+1)} + E_{i\rightarrow{\rm vac}}^{(N-1)} - 2E_{\rm ref}^{(N)} = 0 \tag{3}$$

is truly satisfied and the energy gap $\Delta\varepsilon_{\rm gap}$ becomes zero in an exact manner.

A simple derivation of EQPT is given in Appendix B. Starting with the electronic part of the time-dependent Schrödinger (TDS) equation, and using the definition of the stationary QP wavefunctions (also called *overlap amplitudes*) $\varphi_\alpha^{\rm QP}(\mathbf{r};\mathbf{R}(t),t)$ in Eq. (B1), one can obtain the time-dependent quasiparticle (TDQP) equation,

$$\begin{aligned} \mathrm{i}\frac{\partial}{\partial t}\varphi_\alpha(\mathbf{r};\mathbf{R}(t),t) &= \left(-\frac{1}{2}\nabla_{\mathbf{r}}^2 + v(\mathbf{r},\mathbf{R}(t))\right)\varphi_\alpha(\mathbf{r};\mathbf{R}(t),t) \\ &\quad + \int \Sigma(\mathbf{r},\mathbf{r}';\varepsilon_\alpha^{\rm QP})\,\varphi_\alpha(\mathbf{r}';\mathbf{R}(t),t)\,\mathrm{d}\mathbf{r}' \\ &= \mathscr{H}^{\rm QP}(\mathbf{r};\mathbf{R}(t))\,\varphi_\alpha(\mathbf{r};\mathbf{R}(t),t) \\ &= \varepsilon_\alpha^{\rm QP}\varphi_\alpha(\mathbf{r};\mathbf{R}(t),t), \end{aligned} \tag{4}$$

where $\alpha = i$ or a and $\mathscr{H}^{\rm QP}(\mathbf{r};\mathbf{R}(t))$ is the QP Hamiltonian,

$$\mathscr{H}^{\rm QP}(\mathbf{r};\mathbf{R}(t)) = -\frac{1}{2}\nabla_{\mathbf{r}}^2 + v(\mathbf{r},\mathbf{R}(t)) + \lim_{\mathbf{r}'\rightarrow\mathbf{r}}\int \mathrm{d}\mathbf{r}\;\Sigma(\mathbf{r}',\mathbf{r};\varepsilon_\alpha^{\rm QP}), \tag{5}$$

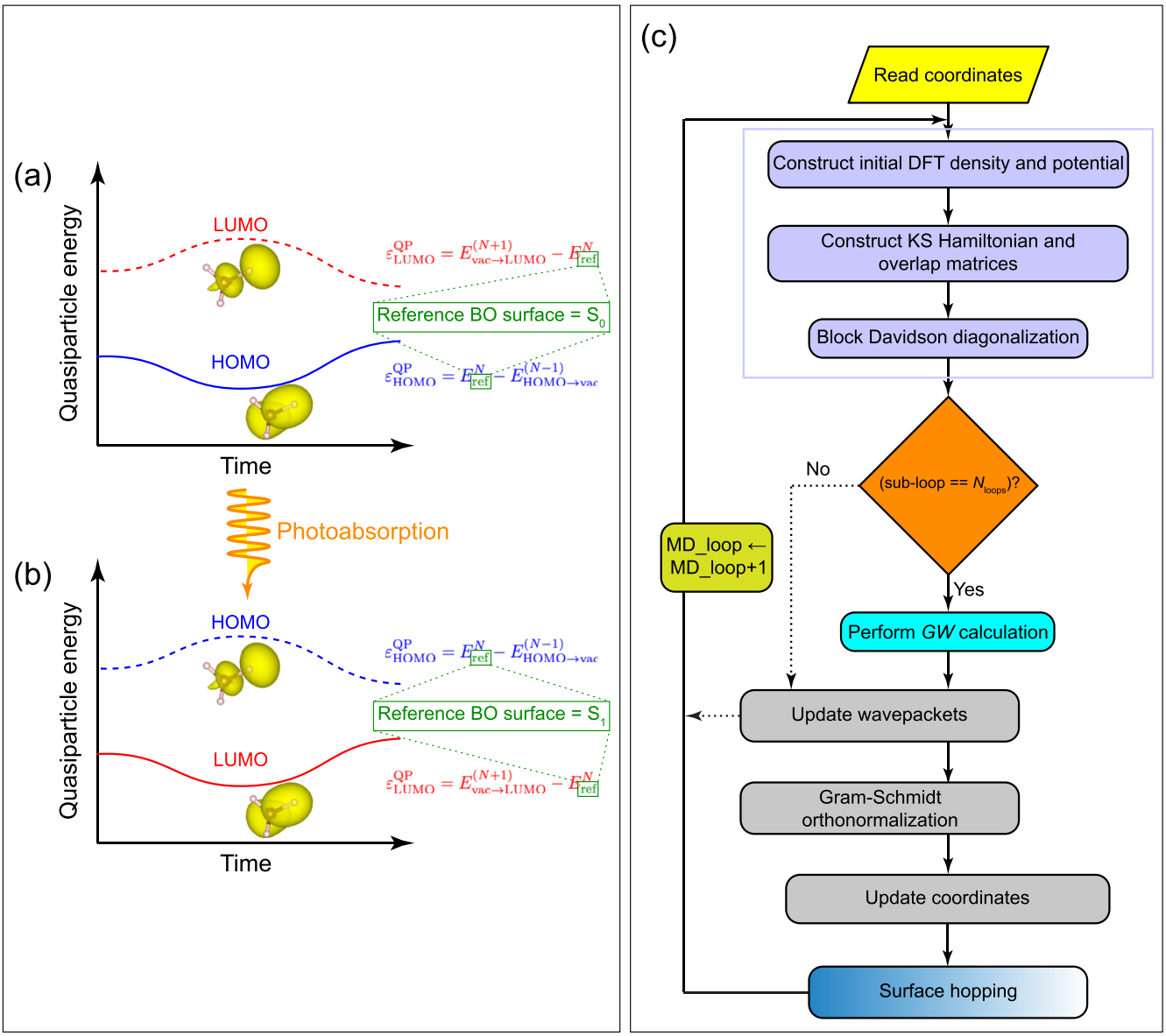

FIG. 1. Schematic and flowchart showing the significance and workflow, respectively, of the NA-ES-TD*GW*-MD method based on EQPT. Panels (a) and (b) show illustrations of the time evolution of the frontier levels in the ground state S_0 and photoexcited state S_1, respectively, of a system. The reference states with respect to the total energy differences that are computed can be either (a) the ground state S_0 or (b) the photoexcited state S_1. Panel (c) shows the flowchart of NA-ES-TD*GW*-MD. At the end of the N_{loops}th electronic sub-loop, a one-shot *GW* calculation is performed (denoted by the blue-colored block) to update the QP energies, subsequent to which the wavepackets and coordinates are updated (denoted by the gray-colored blocks) before entering the next main MD loop. The wavepackets are Gram–Schmidt orthonormalized. Surface hopping is performed after updating the coordinates based on the breaking acceleration condition [Eq (23)].

with $v(\mathbf{r}, \mathbf{R}(t))$ being the external potential describing the Coulomb interaction between the electrons and nuclei and $\Sigma(\mathbf{r}, \mathbf{r}'; \varepsilon^{\mathrm{QP}})$ being the Fourier-transformed self-energy $\Sigma(\mathbf{r}, \mathbf{r}'; t - t')$ in Eqs. (B7) and (B8), which includes all the effects of the electron–electron Coulomb interaction. From Eqs (B4) and (B5), one can conceive that the QP Hamiltonian [Eq. (5)] is the difference between N and $(N \pm 1)$ electron MB electronic Hamiltonians.

As shown in Fig. 1(a), the reference state (labeled by "ref" in Fig. 1) is the ground state, whereas, in Fig. 1(b), it is the photoexcited state. Therefore, the TDQP in Eq. (4) can be applied to any system that starts from an arbitrary (stationary) excited eigenstate. *GW*A under EQPT guarantees that the *GW* QP energies are directly related to the total energies of the excited N and $(N \pm 1)$electron states through Eqs. (1) and (2).

The NA-ES-TD*GW*-MD formalism

We use the exact factorization of the total TDS equation [Eq. (A1)] presented briefly in Appendix A and the transformation of the electronic TDS equation to the TDQP equation [Eq. (4)] valid for any ground/excited eigenstate under EQPT, presented in Appendix B, to develop our NA-ES-TD*GW*-MD formalism for the dynamics. In order to treat the wavepackets $\phi_\lambda(\mathbf{r};\,\mathbf{R}(t),t)$ for studying the electron dynamics, it is necessary to extend the description of Eq. (5) from pure states to mixed states by introducing a summation with respect to α. The QP Hamiltonian for the mixed states can then be written as

$$\begin{aligned}\mathscr{H}^{\mathrm{QP}}_{\mathrm{mixed}}(\mathbf{r};\mathbf{R}(t)) &= -\frac{1}{2}\nabla^2_{\mathbf{r}} + v(\mathbf{r},\mathbf{R}(t)) \\ &\quad + \sum_\alpha \left(\int \mathrm{d}\mathbf{r}'\, \Sigma(\mathbf{r},\mathbf{r}';\varepsilon^{\mathrm{QP}}_\alpha)\, \varphi^{\mathrm{QP}}_\alpha(\mathbf{r}';\mathbf{R}(t)) \right) \\ &\quad \times \int \mathrm{d}\mathbf{r}\, \varphi^{\mathrm{QP}*}_\alpha(\mathbf{r};\mathbf{R}(t)),\end{aligned} \tag{6}$$

where the integral with respect to $\mathbf{r}$ does not operate on the self-energy. The wavepackets $\phi_\lambda(\mathbf{r};\,\mathbf{R}(t),t)$ are normalized to unity,[58] similar to the Kohn–Sham (KS) wavepackets in TDDFT.[3] Therefore, the TDQP equation for $\phi_\lambda(\mathbf{r};\,\mathbf{R}(t),t)$,

$$\mathrm{i}\frac{\partial}{\partial t}\phi_\lambda(\mathbf{r};\mathbf{R}(t),t) = \mathscr{H}^{\mathrm{QP}}_{\mathrm{mixed}}(\mathbf{r};\mathbf{R}(t))\,\phi_\lambda(\mathbf{r};\mathbf{R}(t),t) \tag{7}$$

is identical to the TD Kohn–Sham (TDKS) equation. Instead of directly using the electronic TDS in Eq. (A8), we can use the electronic TDQP in Eq. (4), which is easily derived from the electronic TDS equation, as shown in Eqs. (B4) and (B5). The electronic TDQP equation for the dynamics [Eq. (7)] is obtained by replacing the stationary QP wavefunction $\varphi^{\mathrm{QP}}_\alpha(\mathbf{r};\{\mathbf{R}_I(t)\},t)$ with the wavepacket $\phi_\lambda(\mathbf{r};\,\mathbf{R}(t),t)$ in Eq. (4).

The TDQP equation for dynamics [Eq. (7)] can be formally integrated over a small time interval Δt as

$$\begin{aligned}\phi_\lambda(\mathbf{r};\mathbf{R}(t),t+\Delta t) &= \exp\left[-\mathrm{i}\int_t^{t+\Delta t} \mathscr{H}^{\mathrm{QP}}_{\mathrm{mixed}}(\mathbf{r};\mathbf{R}(t))\,\mathrm{d}t\right] \\ &\quad \times \phi_\lambda(\mathbf{r};\mathbf{R}(t),t).\end{aligned} \tag{8}$$

Using the spectral method,[7,29] we expand the wavepackets with the QP wavefunctions, which are the eigenvalues of the QP Hamiltonian $\mathscr{H}^{\mathrm{QP}}_{\mathrm{mixed}}(\mathbf{r};\mathbf{R}(t))$ as

$$\phi_\lambda(\mathbf{r};\mathbf{R}(t),t) = \sum_\alpha \varphi^{\mathrm{QP}}_\alpha(\mathbf{r};\mathbf{R}(t))\, c_{\alpha\lambda}(t). \tag{9}$$

Unlike in the dynamics prescription of Makhov *et al.*,[36] where many trajectory basis functions are used to expand the wavepacket, here only one trajectory basis function is used, which essentially corresponds to $\phi_\lambda(\mathbf{r},t)$. Since the QP wavefunctions satisfy the orthonormality condition, the expansion coefficients $c_{\alpha\lambda}(t)$ are calculated as

$$c_{\alpha\lambda}(t) = \langle\, \varphi^{\mathrm{QP}}_\alpha(\mathbf{R}(t)) \,|\, \phi_\lambda(\mathbf{R}(t),t)\,\rangle. \tag{10}$$

When the QP Hamiltonian does not change much during Δt, Eq. (8) can be rewritten as

$$\begin{aligned}\phi_\lambda(\mathbf{r};\mathbf{R}(t),t+\Delta t) &\approx \left[1 - \mathrm{i}\mathscr{H}^{\mathrm{QP}}_{\mathrm{mixed}}(\mathbf{r};\mathbf{R}(t))\Delta t\right]\phi_\lambda(\mathbf{r};\mathbf{R}(t),t) \\ &= \sum_\alpha \left[1 - \mathrm{i}\varepsilon^{\mathrm{QP}}_\alpha \Delta t\right]\varphi^{\mathrm{QP}}_\alpha(\mathbf{r};\mathbf{R}(t))\, c_{\alpha\lambda}(t) \\ &\approx \sum_\alpha \exp\left[-\mathrm{i}\varepsilon^{\mathrm{QP}}_\alpha \Delta t\right]\varphi^{\mathrm{QP}}_\alpha(\mathbf{r};\mathbf{R}(t))\, c_{\alpha\lambda}(t),\end{aligned} \tag{11}$$

while Eqs. (6) and (9)–(11) form the basic framework for the electron dynamics.

However, since the basis functions depend on the nuclear positions, it would be more accurate to take into account the effect of the basis functions changing in time through the temporal change of the nuclear positions. Such a remark was made by Saalmann and Schmidt,[59] Prezhdo and Rossky,[60] and Makhov *et al.*[36] Inserting the expansion 9 in the TDQP in Eq. (4) and taking the inner product with $\left\langle \varphi^{\mathrm{QP}}_\beta(\mathbf{R}(t)) \right|$, we obtain

$$\mathrm{i}\frac{\partial}{\partial t}c_{\beta\lambda}(t) + \mathrm{i}\sum_\alpha c_{\alpha\lambda}(t) \left\langle \varphi^{\mathrm{QP}}_\beta(\mathbf{R}(t)) \right| \frac{\partial}{\partial t} \left| \varphi^{\mathrm{QP}}_\alpha(\mathbf{R}(t)) \right\rangle = \varepsilon^{\mathrm{QP}}_\beta c_{\beta\lambda}(t). \tag{12}$$

Here, $\frac{\partial}{\partial t}c_{\beta\lambda}(t)$ can be written in terms of the Euler forward difference form as

$$\frac{\partial}{\partial t}c_{\beta\lambda}(t) = \frac{c_{\beta\lambda}(t+\Delta t) - c_{\beta\lambda}(t)}{\Delta t}, \tag{13}$$

since Δt is small. Rearranging the terms based on this substitution, we obtain

$$\begin{aligned}c_{\beta\lambda}(t+\Delta t) &\approx \left[1 - \mathrm{i}\varepsilon^{\mathrm{QP}}_\beta \Delta t\right] c_{\beta\lambda}(t) - \Delta t \sum_\alpha c_{\alpha\lambda}(t) \\ &\quad \times \left\langle \varphi^{\mathrm{QP}}_\beta(\mathbf{R}(t)) \right| \frac{\partial}{\partial t} \left| \varphi^{\mathrm{QP}}_\alpha(\mathbf{R}(t)) \right\rangle \\ &\approx \exp\left(-\mathrm{i}\varepsilon^{\mathrm{QP}}_\beta \Delta t\right)\Bigg[c_{\beta\lambda}(t) - \Delta t \sum_\alpha c_{\alpha\lambda}(t) \\ &\quad \times \left\langle \varphi^{\mathrm{QP}}_\beta(\mathbf{R}(t)) \right| \frac{\partial}{\partial t} \left| \varphi^{\mathrm{QP}}_\alpha(\mathbf{R}(t)) \right\rangle \Bigg] \\ &= \exp\left(-\mathrm{i}\varepsilon^{\mathrm{QP}}_\beta \Delta t\right)\Bigg[c_{\beta\lambda}(t) - \Delta t \sum_\alpha c_{\alpha\lambda}(t) \sum_I \dot{\mathbf{R}}_I(t) \\ &\quad \times \left\langle \varphi^{\mathrm{QP}}_\beta(\mathbf{R}(t)) \right| \nabla_{\mathbf{R}_I} \left| \varphi^{\mathrm{QP}}_\alpha(\mathbf{R}(t)) \right\rangle \Bigg].\end{aligned} \tag{14}$$

The second term inside the square bracket of Eq. (14) is proportional to the nuclear velocity $\dot{\mathbf{R}}_I(t) = d\mathbf{R}_I(t)/dt$ and represents a non-adiabatic interaction.[36,59,60] If we express the wavefunctions by an orthonormal basis set $\xi_i(\mathbf{r};\,\mathbf{R}(t))$ as

$$\varphi^{\mathrm{QP}}_\alpha(\mathbf{r};\mathbf{R}(t)) = \sum_i a_{\alpha i}\, \xi_i(\mathbf{r};\mathbf{R}(t)), \tag{15}$$

we have

$$\left\langle \varphi^{\mathrm{QP}}_\beta(\mathbf{R}(t)) \right| \nabla_{\mathbf{R}_I} \left| \varphi^{\mathrm{QP}}_\alpha(\mathbf{R}(t)) \right\rangle = \sum_{ij} a^*_{\beta i}\, \mathbf{d}_{ij}(\mathbf{r};\mathbf{R}(t))\, a_{\alpha j}, \tag{16}$$

where $\mathbf{d}_{ij}(\mathbf{r};\,\mathbf{R}(t))$ is the non-adiabatic coupling vector defined by[37]

$$\mathbf{d}_{ij}(\mathbf{r};\mathbf{R}(t)) = \langle \xi_i(\mathbf{R}(t)) \,|\, \nabla_{\mathbf{R}_I} \,|\, \xi_j(\mathbf{R}(t)) \rangle. \tag{17}$$

We employ Eqs. (14)–(17) in our simulations because of their high accuracy.

Now, we apply this formalism to the one-shot *GW* approach,[61] which is the simplest approach in the *GW* approximation in MBPT. In the one-shot *GW* approach, the QP eigenfunctions are replaced by the LDA eigenfunctions as

$$\varphi_\alpha^{\mathrm{QP}}(\mathbf{r};\mathbf{R}(t)) \approx \varphi_\alpha^{\mathrm{LDA}}(\mathbf{r};\mathbf{R}(t)), \tag{18}$$

and the QP energy eigenvalues $\varepsilon_\alpha^{\mathrm{QP}}$ are calculated from the LDA eigenvalue $\varepsilon_\alpha^{\mathrm{LDA}}$ and exchange–correlation potential $\mu_{\mathrm{xc}}^{\mathrm{LDA}}(\mathbf{r})$ as[61]

$$\varepsilon_\alpha^{\mathrm{QP}} \approx \varepsilon_\alpha^{\mathrm{LDA}} + \left\langle \varphi_\alpha^{\mathrm{LDA}}(\mathbf{R}(t)) \middle| \left[\Sigma_{\mathrm{xc}}(\varepsilon_\alpha^{\mathrm{QP}}) - \mu_{\mathrm{xc}}^{\mathrm{LDA}} \right] \middle| \varphi_\alpha^{\mathrm{LDA}}(\mathbf{R}(t)) \right\rangle, \tag{19}$$

where $\Sigma_{\mathrm{xc}}(\varepsilon_\alpha^{\mathrm{QP}})$ is the exchange–correlation part of the self-energy, which does not include the Hartree term. The self-energy $\Sigma_{\mathrm{xc}}(\varepsilon_\alpha^{\mathrm{QP}})$ in Eq. (19) explicitly depends on the resulting QP energy $\varepsilon_\alpha^{\mathrm{QP}}$. However, this is not a problem because the QP energy obtained in the previous time step can be used as the argument of the self-energy in the present time step. As a result, the renormalization procedure is not needed in the present time-dependent approach. The usage of the QP energies $\varepsilon_\alpha^{\mathrm{QP}}$, which are obtained by Eq. (19) in Eq. (11) or Eq. (14) is the distinguishing feature of our TD*GW* approach. Except for this difference, everything else remains the same as in the TDDFT dynamics formulation. The Newtonian equation of motion for NA-ES-TD*GW*-MD is identical to Eq. (A9),

$$\begin{aligned} M_I \frac{\mathrm{d}^2\mathbf{R}_I(t)}{\mathrm{d}t^2} &= -\nabla_{\mathbf{R}_I} \left\langle \Psi_{\mathrm{ref}}^{(N)}(\mathbf{R}(t),t) \middle| \hat{\mathscr{H}}_{\mathrm{MB}}(\mathbf{R}(t)) \middle| \Psi_{\mathrm{ref}}^{(N)}(\mathbf{R}(t),t) \right\rangle \\ &= -\nabla_{\mathbf{R}_I} E_{\mathrm{ref}}^{(N)}(\mathbf{R}(t),t) \\ &\approx -\nabla_{\mathbf{R}_I} E_{\mathrm{LDA}}^{(N)}(\mathbf{R}(t),t), \end{aligned} \tag{20}$$

where $\left|\Psi_{\mathrm{ref}}^{(N)}(\mathbf{R}(t),t)\right\rangle$, $E_{\mathrm{ref}}^{(N)}(\mathbf{R}(t),t)$, and $E_{\mathrm{LDA}}^{(N)}(\mathbf{R}(t),t)$ are the electronic wavefunction, the true *GW* total electronic energy, and the approximate LDA total electronic energy of a N-electron reference state (ground state or excited eigenstate), respectively. Although the exchange–correlation contribution to $E_{\mathrm{LDA}}^{(N)}(\mathbf{R}(t),t)$ is approximated by its LDA form, the wavepackets used for time-dependent charge densities are updated by Eq. (11) or alternatively Eq. (14). Therefore, $E_{\mathrm{LDA}}^{(N)}(\mathbf{R}(t),t)$ is not the simple LDA total electronic energy, but it includes the QP effects via the QP Hamiltonian $\hat{\mathscr{H}}_{\mathrm{mixed}}^{\mathrm{QP}}(\mathbf{R}(t))$.

Ab initio cloning in NA-ES-TD*GW*-MD

From Eqs. (A9) and (20), the nuclear trajectory evolves as the gradient of the average potential generated by the electrons, making the Ehrenfest approach a mean-field approach. With such a mean-field approximation, the correlation (also known as *quantum coherence*) between the electron "motion" and nuclear trajectory is neglected. This leads to a problem of the system continuing to evolve on the average potential after having left a region of strong nonadiabatic mixing without collapsing onto one of the BO surfaces. In other words, a proper description of such correlations requires a distinct classical trajectory for each electronic state, which is provided by an SH strategy, such as that proposed by Tully[30,31,62,63] and Makhov *et al.*[36] We adopt the SH strategy proposed by Makhov *et al.*,[36] named *ab initio* (multiple) cloning in our dynamics formalism (although our approach does not include multiple trajectory basis functions).

A quantity that is used as a measure of quantum (de)coherence, i.e., hopping *from* a mixed surface (with index λ) *to* a pure BO surface (with index α) is called the "breaking force". This is defined as

$$\mathbf{F}_{\lambda\to\alpha}^{\mathrm{br}}(t) = \left(1 - |c_{\alpha\lambda}(t)|^2\right) \Delta\mathbf{F}_{\alpha\lambda}(t), \tag{21}$$

where $c_{\alpha\lambda}(t)$ is the coefficient expansion of the wavepacket $\phi_\lambda(\mathbf{r},t)$ as defined in Eq. (10) and $\Delta\mathbf{F}_{\alpha\lambda}(t)$ is the deviation of the force felt by the nuclei when traversing one of the BO surfaces (also known as *BO force*) from the mean-field force obtained from Eq. (20) (also known as *Ehrenfest force*), i.e.,

$$\Delta\mathbf{F}_{\alpha\lambda}(t) = \nabla_{\mathbf{R}_I} E_\lambda^{(N)}(\mathbf{R}(t),t) - \nabla_{\mathbf{R}_I} E_\alpha^{(N)}(\mathbf{R}(t),t), \tag{22}$$

where $E_\alpha^{(N)}(\mathbf{R}(t),t)$ and $E_\lambda^{(N)}(\mathbf{R}(t),t)$ are the LDA total electronic energies of the BO surface α and the Ehrenfest "surface" λ, respectively. $\Delta\mathbf{F}_{\alpha\lambda}(t)$ provides an indication of the hop, if the Ehrenfest force [second term in Eq. (22)] deviates significantly from the BO force [first term in Eq. (22)] for a given time t. The condition for a hop (or "clone" in Ref. 36) is that the breaking acceleration is greater than a pre-decided threshold δ_{clone},

$$a_{\lambda\to\alpha}^{\mathrm{br}}(t) = |\mathbf{M}^{-1}\mathbf{F}_{\lambda\to\alpha}^{\mathrm{br}}(t)| > \delta_{\mathrm{clone}}. \tag{23}$$

In this work, we define $\delta_{\mathrm{clone}} = 3 \times 10^{-6}$ a.u. for exploring the surface hop time for CH_4.

The workflow of NA-ES-TD*GW*-MD in TOMBO

Since the eigenstates span the complete Hilbert space, we use the all-electron mixed-basis approach[7,29,64,65] implemented in our home-grown *ab initio* package named Tohoku mixed basis orbitals (TOMBO),[66] in which the one-electron orbitals are expressed by both plane waves (PWs) and atomic orbitals (AOs). So far, this code has been applied to various *GW* calculations at the ground state[67,68] and also to the excited states.[25–27] We use a simple cubic unit cell of 12 Å, where the Coulomb interaction is spherically cut to avoid interactions with adjacent unit cells. 14 147 PWs corresponding to the 17.3 Ry cutoff energy are used with minimal number of numerical AOs, which have finite values only within each nonoverlapping atomic sphere. The AOs are smoothly truncated by subtracting a smooth quadratic function, which has the same amplitude and derivative at the atomic sphere surface.[66] This quadratic function smoothly connecting to the tail of the true orbital (outside this nonoverlapping atomic sphere) can be successfully described by a linear combination of PWs. The cutoff energies for the exchange and correlation parts of the self-energy are set to 69 Ry and 7.7 Ry, respectively. 50 levels are used in the spectral decomposition of Eq. (11) and in the calculation of the correlation part of the self-energy. The generalized plasmon pole model is used to avoid frequency integration.[61] We performed tests to ensure that all these parameters are sufficient for obtaining good convergence of results. However, we increased the cutoff energies to 44 Ry (for PWs), 123 Ry (for exchange), and 11 Ry (for correlation) as well as the number of levels to 4600 whenever separate single-shot *GW* calculations were performed.

The workflow of a TD*GW* simulation is shown in Fig. 1(c). First, the initial coordinates are read (yellow-colored block) and the one-electron states are converged at a given electron configuration within the LDA level (lavender-colored blocks). The results

may certainly improve if the LDA functional is changed to other hybrid or range-separated functionals. However, the time required for convergence with LDA is much lesser than that with these more sophisticated functionals, and hence, we only use LDA in our study. Once convergence is achieved, the TD*GW* dynamics is initiated. A time step of $\Delta t = 0.01$ fs is used in Eqs. (12)–(14) and (20) as we found this interval to be sufficiently small such that the Hamiltonian changes gradually. For every atomic position update, we perform N_{loops} sub-loops to update the time-dependent one-electron states in Eq. (11) within the LDA level, followed by the *GW* calculation at the end of the N_{loops}th sub-loop. In other words, the QP energies are updated (light-blue-colored block) only after the N_{loops}th sub-loop (orange-colored block). [One could thin out the number of one-shot *GW* calculations to reduce the computational time. For example, one could perform such one-shot *GW* calculations to correct for the (QP) energies every 10 MD loops. However, we do not use this technique in the present work since we can afford the computational cost for CH_4 within the wall time limits of the presently available supercomputing resources.] For the remaining $N_{\text{loops}} - 1$ sub-loops, the wavepackets are updated (gray-colored block) using the non-updated QP energies in Eq. (14). Once done, these wavepackets are orthonormalized using the Gram–Schmidt orthonormalization scheme.[69] Subsequently, the atomic positions are updated using Eq. (A9) (gray-colored block). This is the conventional Newtonian equation of motion supplemented with the quantum force calculated as the negative gradient of the expectation value of the MB Hamiltonian, $\mathscr{H}_{\text{MB}}(\mathbf{r};\mathbf{R}(t))$. We use a variational force for this derivative, as formulated by Ho *et al.*[70] The N_{loops} ($N_{\text{loops}} = 20$ for TOMBO) sub-loops ensure that the total energy is nearly conserved as we perform NVE simulations. Surface hopping is performed based on whether the breaking acceleration exceeds a pre-defined tolerance value or not, as per Eq. (23). The LDA eigenvalue problem is solved by using the block Davidson method.[71] *GW* is known to scale as $\sim\mathcal{O}(N_{\text{B}}^4)$ with N_{B} being the number of basis functions, while DFT with LDA scales as $\sim\mathcal{O}(N_{\text{B}}^3)$. Since *GW* is executed only once at the N_{loops}th step, the overall cost of our NA-ES-TD*GW*-MD approach is a weighted average of $\sim\mathcal{O}(N_{\text{B}}^{3-4})$, which is the same as that of TDDFT-MD. Therefore, we can obtain more accurate energies using NA-ES-TD*GW*-MD and hence, a better understanding of such photochemical reactions at virtually the same cost as TDDFT-MD.

RESULTS

The ground state structure of methane (CH_4) is shown in Fig. S1 in the supplementary material. Applying *GW*A to the neutral ground state, we obtained 13.7 ± 0.5 eV and -0.9 ∓ 0.5 eV for ionization potential (IP) and electron affinity (EA) of CH_4, respectively (see "Singlet Excitation/*GW*" presented in Table I). Our error estimation presented in Table I is based on the variation in the results depending on our choice of the reference state, for example, we can evaluate IP using either the ground state (to remove one electron) or the cationic state (to add one electron). Our IP is within the wide energy range of 12.6–14.8 eV provided by experimental observations.[46,72,73] We estimated EA by linearly extrapolating to 1/unit cell size → 0 as proposed in Ref. 68.

Moreover, applying the *GW* method to CH_4^+ without solving the Bethe–Salpeter equation,[25] we obtain 9.5 ± 0.5 eV as the photoabsorption energy (PAE) of CH_4 (see "Singlet Excitation/*GW*" presented in Table I). Previously calculated vertical excitation energies of the first singlet excited S_1 ($^1T_2$) and first triplet excited T_1 ($^3T_2$) states are in the range of 10.41–10.91 eV[44,45] and 10.08–10.43 eV[44] using multi-reference wavefunction-based methods, while the experimental PAE is around 10.2 eV.[46–50] Our one-shot *GW* value of 9.5 ± 0.5 eV is in good agreement with 10.2 eV. Depending on the amount of photoexcitation, several dissociation mechanisms have been proposed.[48–53] Many of these are spin-conserving and merely undergoing internal conversion (IC) to the ground state of the products, with some of them undergoing intersystem crossing (ISC) that may lead to the same products[44–46,49] (Table II).

The excitation from the ground-state S_0 to the singlet excited-state S_1 manifold is modeled by a HOMO ($1t_2$) → LUMO ($3s$) transition of an electron[45–50,74] (HOMO: highest occupied molecular orbital and LUMO: lowest unoccupied molecular orbital). Subsequent to this excitation, the dynamics can be propagated on S_1. However, the Ehrenfest dynamics fails in cases where a surface crossing is involved. Due to the mean-field nature of Ehrenfest MD, we do not obtain a correct description of the C– H dissociation process in CH_4 (see Fig. S2 in the supplementary material). This problem can be mitigated by including non-adiabaticity via surface hopping in the dynamics formulation. When the breaking acceleration becomes larger than a pre-defined acceleration tolerance (see METHODS), a surface hop to a BO state is performed.[36]

TABLE I. Summary of important energies (intercepts) at $t = 0$. The energies listed in the table are ionization potential (IP), electron affinity (EA), photoabsorption energy (PAE), and the frontier QP levels OCC1 and EMP1. The values inside the parentheses are those obtained using $\varepsilon_{\text{OCC1}} = \text{PAE} - \text{IP}$ and $\varepsilon_{\text{EMP1}} = -\text{PAE} - \text{EA}$.

System →	Singlet excitation [with ground state geometry]		Triplet excitation [with geometry in Fig. S6(b)]
Energy (eV) →	*GW*	Experiment	*GW*
$\text{IP} = E_{\text{HOMO}\to\text{vac}}^{(N-1)} - E_{\text{GS}}^{(N)}$	13.7 ± 0.5	12.6–14.8[a]	13.8 ± 0.5
$\text{EA} = E_{\text{GS}}^{(N)} - E_{\text{vac}\to\text{LUMO}}^{(N+1)}$	-0.9 ∓ 0.5	⋯	-0.8 ∓ 0.5
PAE	9.5 ± 0.5	10.2[b]	9.4 ± 0.4
$\varepsilon_{\text{OCC1}}(= \text{PAE} - \text{IP})$	-4.2, α-spin (-4.2 ∓ 0.5)	(2.4–4.6)	-4.3, α-spin (-4.4 ∓ 0.5)
$\varepsilon_{\text{EMP1}}(= -\text{PAE} - \text{EA})$	-8.3, α-spin (-8.6 ∓ 0.5)	⋯	-8.3, β-spin (-8.6 ∓ 0.5)

[a]IP values from the literature[46,72,73]
[b]PAE value from the literature.[46–50]

TABLE II. Energies (in eV) of important occupied orbitals at t = 34 fs (t = 20 fs) for the singlet (triplet) excitation pathway of dissociation, obtained from NA-ES-TD*GW*-MD simulations. For the singlet excitation spin-preserved (spin-swap) channel, $A = \beta$ (α) and $B = \alpha$ (β), and for triplet excitation, $A = \alpha$ and $B = \beta$. The energies of four different systems–$CH_3^\bullet$ + H [2nd and 7th rows, Fig. S3 (singlet)/S8 (triplet) in the supplementary material], isolated $CH_3^\bullet$ with geometry the same as that of the $CH_3^\bullet$ fragment at t = 34/t = 20 fs [3rd and 8th rows, Fig. S4 (singlet)/S7 (triplet)], isolated planar $CH_3^\bullet$ [4th (comp.)/5th (exp.) and 9th (comp.)/10th (exp.) rows, Fig. S5], and isolated H (6th and 11th rows) for the singlet/triplet excitation pathway of dissociation. The orbitals in the parenthesis in rows 3, 6, 8, 9, 10, and 11 indicate those of the corresponding isolated systems.

		A-spin				*B*-spin	
Pathway	System	ε_{OCC4}	ε_{OCC3}	ε_{OCC2}	ε_{OCC1}	ε_{OCC2}	ε_{OCC1}
Singlet excitation	$CH_3^\bullet$ + H at t = 34 fs	−23.7 −17.33[c]	−15.7 −11.55[c]	−14 −9.84[c]	−9 −5.46[c]	−13.5 −9.39[c]	−13.2 −7.61[c]
	$CH_3^\bullet$ geometry at t = 34 fs	−22.8 −17.22[c]	−16.3 −11.45[c]	−14.5 −9.77[c]	−9.8 −5.38[c]	−14.1 −9.32[c] (HOMO)	
	Planar $CH_3^\bullet$	−22.3 −16.81[c]	−15.1 −10.36[c]	−15.1 −10.36[c]	−9.7 −5.31[c]	−14.7 −9.92[c]	
	Planar $CH_3^\bullet$ (experimental)[a]	−24.57	−15.64	−15.64	−9.84	−15.64	
	Isolated H atom	...	...	...	...	...	−13.2 −13.6[b] −7.85[c] (HOMO)
Triplet excitation	$CH_3^\bullet$ + H at t = 20 fs	−14.4 −10.22[c]	−13.8 −9.62[c]	−13.6 −8.07[c]	−10.7 −6.67[c]	−13.8 −9.75[c]	−13.1 −9.15[c]
	$CH_3^\bullet$ geometry at t = 20 fs	−14.8 −10.09[c] (HOMO−2)	−14.2 −9.53[c] (HOMO−1)		−11.1 −6.49[c] (HOMO)	−14.4 −9.05[c] (HOMO−1)	−13.8 −9.62[c] (HOMO)
	Planar $CH_3^\bullet$	−15.1 −10.36[c] (HOMO−2)	−15.1 −10.36[c] (HOMO−1)		−9.7 −5.31[c] (HOMO)	−14.7 −9.92[c] (HOMO−1)	−14.7 −9.92[c] (HOMO)
	Planar $CH_3^\bullet$ (experimental)[a]	−15.64 (HOMO−2)	−15.64 (HOMO−1)		−9.84 (HOMO)	−15.64 (HOMO−1)	−15.64 (HOMO)
	Isolated H atom	...	...	−13.2 −13.6[b] −7.85[c] (HOMO)		...	...

[a]From Ref. 75.
[b]From Ref. 76.
[c]LDA computed energy eigenvalues.

For this, we continue our NA-ES-TD*GW*-MD simulation of the singlet excitation at this switching time by (a) choosing the geometry of methane slightly after the crossing point, (b) using the momentum of a previous time step, and (c) running the simulation for three channels, spin-preserved (singlet), spin-swap (singlet), and spin-flip (triplet). In addition to the singlet excitation with spin-preserved/spin-swap/spin-flip channel, we also perform a simulation of a triplet excitation, as it is reported to be an alternative (albeit slower) mechanism.[44,46]

Singlet excitation

The photoexcitation process involves pumping an α-spin ($\uparrow$-spin) electron from a bonding orbital $HOMO_\alpha$ to an antibonding orbital $LUMO_\alpha$. With this, $HOMO_\alpha$ becomes unoccupied while $LUMO_\alpha$ is occupied. This initiates the dissociation process. The amount of photoexcitation provided for the HOMO → LUMO excitation is sufficient to eject one H atom from the system,[45,46,49] eventually leading to $CH_3^\bullet$ and H.

The time evolution of the HOMO−3 to LUMO+3 QP energy levels (obtained from NA-ES-TD*GW*-MD) is shown in Figs. 2(a) and 2(b). The left panel (a) indicates the QP energies of α-spin ($\uparrow$-spin) orbitals, while the right panel (b) indicates the β-spin ($\downarrow$-spin) ones. As mentioned above, the ordering of $HOMO_\alpha$ and $LUMO_\alpha$ is swapped and these orbitals are termed as "EMP1" (thick orange dotted–dashed line) and "OCC1" (thick blue dashed line), respectively, as shown in Fig. 2(a). The labels such as $OCC\#_{\alpha/\beta}$ and

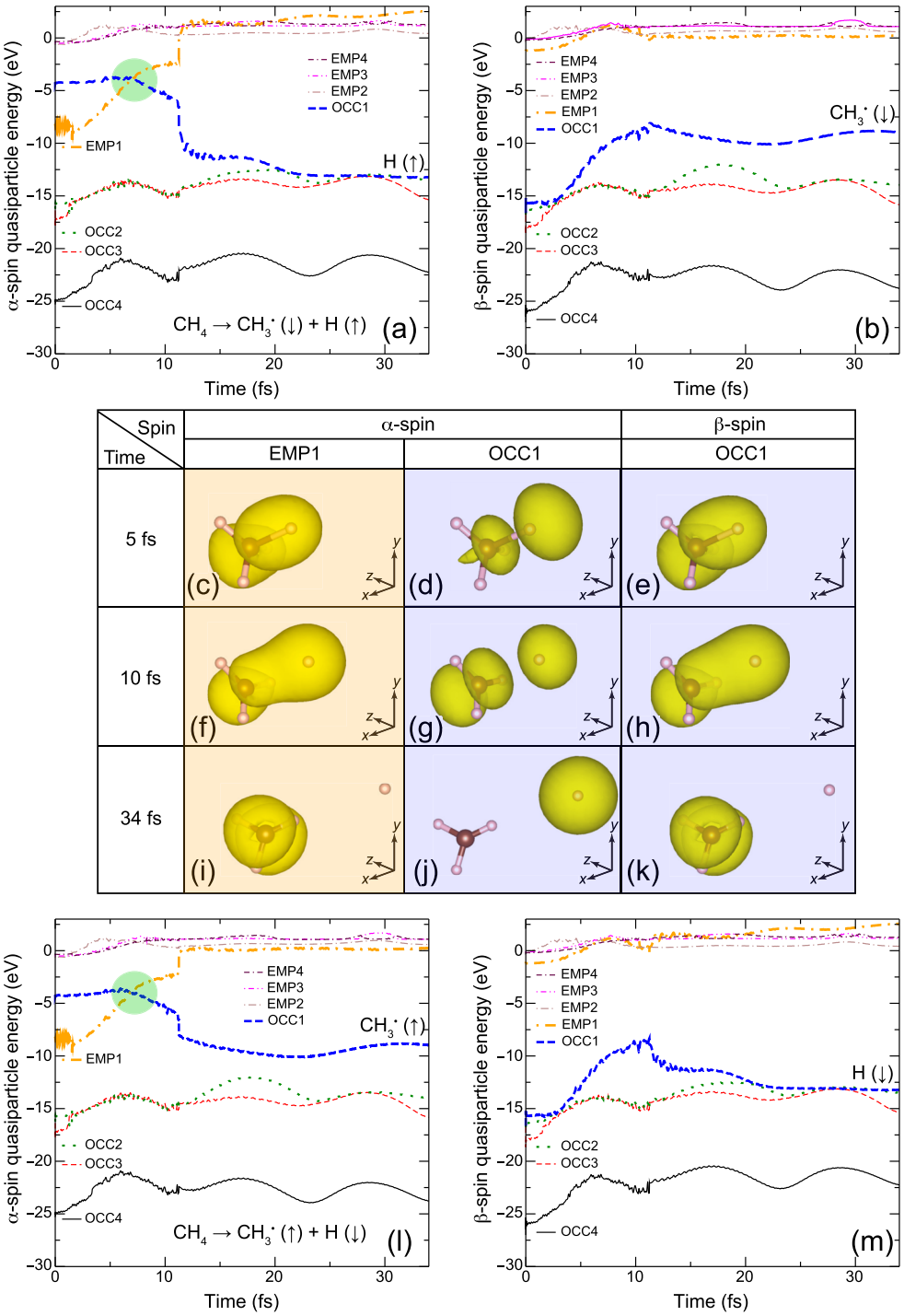

FIG. 2. Temporal change of QP energies and charge densities for the spin-preserved and spin-swap channel simulations. Evolution of the QP energies of (a) α and (b) β spins with time obtained from NA-ES-TD*GW*-MD for the spin-preserved channel. The green-shaded region in panel (a) denotes the region of crossing between $OCC1_\alpha$ and $EMP1_\alpha$. Panels (c)–(k) indicate the charge densities of $EMP1_\alpha$, $OCC1_\alpha$, and $OCC1_\beta$ at $t = 5$ fs [panels (c) and (d) for α, and (e) for β], $t = 10$ fs [panels (f) and (g) for α, and (h) for β], and $t = 34$ fs [panels (i) and (j) for α, and (k) for β]. The colors of each of these panels correspond to the colors of the levels in panels (a) and (b). The isosurface for the charge density plots was set at 1×10^{-8} electrons/Å^3. The directions of viewing are indicated for reference. Panels (l) and (m) indicate the evolution of QP energies of α and β spins, respectively, with time for the spin-swap channel.

EMP#$_{\alpha/\beta}$, with # = 1, 2, . . . to indicate the lower occupied and higher empty levels, respectively, are also shown in Fig. 2. The QP energies $\varepsilon_{OCC1_\alpha}$ and $\varepsilon_{EMP1_\alpha}$ at $t = 0$ [intercepts in Fig. 2(a)] are listed in "singlet excitation/*GW*" presented in Table I.

The C–H bond separation process begins with the recoil received by the CH_3 group from the ejection of the H atom, as a result of the transition of an electron from the bonding to the antibonding orbital. For $t < 7$ fs, the $EMP1_\alpha$ level is bonding-like, while the $OCC1_\alpha$ level is antibonding-like, as shown in the charge density plots for these two levels shown in Figs. 2(c) and 2(d) at $t = 5$ fs. (Hereafter, "charge density" implies the absolute value of the QP wavefunction-squared irrespective of its occupancy.) With time, these two levels approach and cross at $t = 7$ fs [green-shaded region shown in Fig. 2(a)]. The crossing between the levels is indicative of the crossing between the S_1 surface that we start with and the new S_0 adiabatic surface of the ground state. The simulation with the spin-preserved channel is continued at the surface hopping (SH) time $t = 11.25$ fs, where the breaking acceleration exceeds the threshold value $\delta_{clone} = 3 \times 10^{-6}$ a.u. (see METHODS). Here, the H atom is separated even more from the methyl fragment (C– H bond distance = 2.4 Å) than at the crossing point (C– H bond distance = 1.7 Å). The geometry and momentum at a previous time $t = 11.24$ fs are used for the subsequent spin-preserved run. We impart ↑ and ↓ spins to the H and methyl fragments, respectively, and define this configuration as the new BO surface after the transition.

The levels show a discontinuity at $t = 11.26$ fs because of the transition from the S_1 to the new S_0 surfaces of the $CH_3^\bullet\downarrow + H\uparrow$ combined system. Beyond this SH point, the H atom continues to move away from the methyl fragment. Toward the end of this simulation, at around $t = 34$ fs, $OCC1_\alpha$ clearly represents the isolated H 1*s* atomic state in terms of both its charge density [Fig. 2(j)] and energy [−13.2 eV shown in Fig. 2(a) and Fig. S3(dα) in the supplementary material and the "Singlet excitation" presented in Table II, *B*-spin of ε_{OCC1}], which is close to the exact value of −13.6 eV for the isolated H obtained experimentally.[76] At the same time, the lower three occupied levels, $OCC2_{\alpha/\beta}$ [Fig. S3(cα)/(cβ)], $OCC3_{\alpha/\beta}$ [Fig. S3(bα)/(bβ)], and $OCC4_{\alpha/\beta}$ [Fig. S3(aα)/(aβ)] reflect the isolated $CH_3^\bullet$ radical (with the same geometry as in the simulation at $t = 34$ fs) states $HOMO_\beta$/$HOMO-1_\alpha$ [Fig. S4(cβ)/(cα)], $HOMO-1_\beta$/$HOMO-2_\alpha$ [Fig. S4(bβ)/(bα)], and $HOMO-2_\beta$/$HOMO-3_\alpha$ [Fig. S4(aβ)/(aα)], respectively. (This also applies to the comparison between the $OCC2_{\alpha/\beta}$, $OCC3_{\alpha/\beta}$, $OCC4_{\alpha/\beta}$ levels and the corresponding levels in ideal planar $CH_3^\bullet$, as shown in Fig. S5.) The corresponding QP energies are listed together with the LDA energy eigenvalues in the *A*-spin ε_{OCC2}-ε_{OCC4} columns of "Singlet excitation" presented in Table II. On the other hand, we see that $OCC1_\beta$ clearly represents the isolated $CH_3^\bullet$ radical $HOMO_\alpha$ in terms of both its charge density [Fig. 2(k) vs Fig. S4(dα)] and energy [−9 eV in Fig. 2(b) vs −9.8 eV (−9.7 eV) for the isolated $CH_3^\bullet$ radical shown in Fig. S4 (Fig. S5)] listed in the *A*-spin ε_{OCC1} column of "Singlet excitation" presented in Table II. Compared to the LDA energy eigenvalues, the QP energies of all these levels observed at the end of our TD*GW* simulations or obtained through one-shot *GW* calculations are in very good agreement with the experimentally reported values[75] (presented in the fifth row in Table II) demonstrating the immense predictive power of our method.

On the other hand, in the spin-swap channel, ↑ and ↓ spins are imparted to the methyl and H fragments, respectively, and this configuration is considered as the new BO surface after the surface hop. The time evolution of QP levels for the spin-swap channel is shown in Figs. 2(l) and 2(m). Here, the α/β QP energies shown in Figs. 2(a) and 2(b) after the SH time are replaced with the β/α QP energies to obtain Figs. 2(l) and 2(m). As a result, the discussion involving all the results, including those presented in "Singlet excitation" in Table II, is interchanged.

In addition to these spin-preserved and spin-swap channels of the singlet excitation simulation, we also simulate a spin-flip channel where we impart ↑ spins to both the methyl and H fragments by moving one electron from $OCC1_\beta$ to $EMP1_\alpha$ and define this configuration as the new BO surface after the transition, with the previous $^1OCC1_\alpha$ and $^1EMP1_\alpha$ becoming the new $^3OCC2_\alpha$ and $^3OCC1_\alpha$, respectively. The time evolution of the QP energies is shown in Figs. 3(a) and 3(b). The levels at $t > 11.25$ fs (SH time) are appended with "3" in the superscript to denote that they now correspond to the $CH_3^\bullet\uparrow + H\uparrow$ triplet configuration. At $t = 33$ fs, $^3OCC2_\alpha$ [Fig. 3(l)] has −13.6 eV [Fig. 3(a)], which represents the H 1*s* atomic state and $^3OCC1_\alpha$ [Fig. 3(m)] has an energy of −8.9 eV [Fig. 3(a)], which corresponds closely to $HOMO_\alpha$ of the ideal planar $CH_3^\bullet$ radical [−9.7 eV presented in Table II and Fig. S5(dα) in the supplementary material]. In addition, all the β occupied QP levels represent isolated $CH_3^\bullet$ radical states for $t > 11.25$ fs [shown only for $^3OCC1_\beta$ in Figs. 3(f), 3(j), and 3(n) at $t = 18$, 21, and 33 fs, respectively].

Triplet excitation

The alternative pathway to the dissociation process is via the intermediate T_1 surface through an ISC from the S_1 surface. We use the structure from our NA-ES-TD*GW*-MD for the S_1 dissociation pathway at $t = 1.4$ fs, which resembles closely with the reported structure (referred to as X2 in Ref. 44), as the starting point for exploring the triplet pathway. The bond lengths and bond angles of this structure are shown in Fig. S6(b) in the supplementary material along with those reported in Ref. 44, for comparison. We assume that the ISC has taken place and that we are already maneuvering the T_1 ($^3A'$) surface. We estimated IP and the linearly extrapolated EA values by performing *GW* calculations of this initial triplet geometry. Moreover, from a separate *GW* calculation for CH_4^- having an additional α-spin electron, we identified the difference between the singlet and triplet PAEs as $\varepsilon_{HOMO_\beta} - \varepsilon_{HOMO-1_\alpha}$. Then, together with the singlet PAE estimated separately by a *GW* calculation for CH_4^+, we estimated the triplet PAE as 9.4 ± 0.4 eV. All these values are listed under "Triplet Excitation/*GW*" presented in Table I.

We define the system to have a triplet electronic configuration comprising of six α and four β occupied orbitals. All the energy levels of the α and β spin orbitals are now relabeled, for example, $HOMO_\alpha$ as "$OCC2_\alpha$", $LUMO_\alpha$ as "$OCC1_\alpha$", $HOMO_\beta$ as "$EMP1_\beta$", and $HOMO-1_\beta$ as "$OCC1_\beta$" (Fig. 4). The QP energies of $\varepsilon_{OCC1_\alpha}$ and ε_{EMP1_β} at $t = 0$ [intercepts shown in Figs. 4(a) and 4(b)] are listed under "Triplet Excitation/*GW*" in presented Table I.

Initially, $OCC2_\alpha$, $OCC3_\alpha$, and $OCC4_\alpha$ are nearly degenerate [Fig. 4(a)], similar to the corresponding triply degenerate methane sp^3 orbitals, such as the case with $OCC1_\beta$ and $OCC2_\beta$ [Fig. 4(b)]. While the occupied $OCC1_\alpha$ level has a more antibonding character [Fig. 4(d)], the empty $EMP1_\beta$ level is a bonding orbital [Fig. 4(f)]

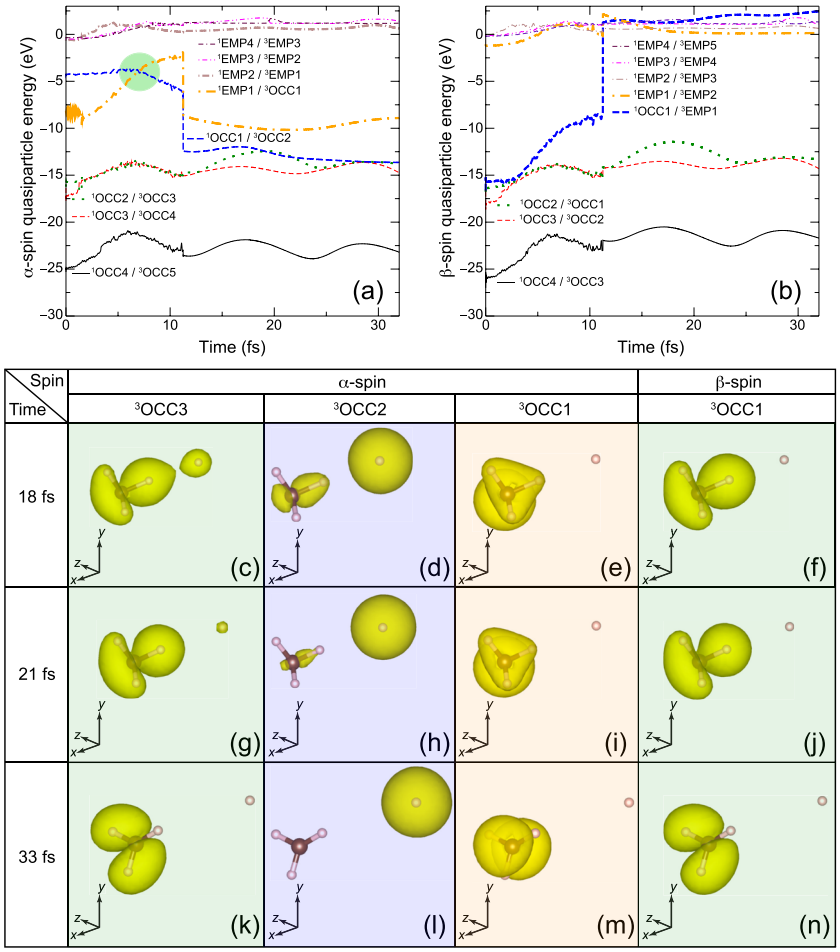

FIG. 3. Temporal change of the QP energies and charge densities for the spin-flip channel simulation. Evolution of QP energies of (a) α and (b) β spins with time, obtained from NA-ES-TD*GW*-MD. The green-shaded region in panel (a) denotes the region of crossing between ^{1}OCC1$_\alpha$ and ^{1}EMP1$_\alpha$. The levels after t = 11.25 fs, in both panels (a) and (b) are from the continued run with the $CH_3^\bullet\uparrow + H\uparrow$ triplet configuration. Therefore, these levels are appended with 3 in the superscript. Panels (c)–(n) show the charge densities for ^{3}OCC3$_\alpha$, ^{3}OCC2$_\alpha$, ^{3}OCC1$_\alpha$, and ^{3}OCC1$_\beta$ levels at t = 18, 21, and 33 fs. The colors of each of these panels correspond to the colors of the levels in panels (a) and (b). The isosurface for the charge density plots was set at 1×10^{-8} electrons/Å^3. The directions of viewing are indicated for reference.

(similar to OCC2$_\alpha$ [Fig. 4(c)]) sharing threefold similarities with OCC1$_\beta$ [Fig. 4(e)] and OCC2$_\beta$. However, since this orbital is unoccupied through ISC, the degeneracy for this orbital is lifted. Therefore, EMP1$_\beta$ gradually increases in energy and moves toward the vacuum level (0 eV) at around 7 fs. At 10 fs, OCC2$_\alpha$ shows charge predominantly localized around the dissociating H atom [Fig. 4(g)]. The temporal change of the ^{3}OCC1$_\alpha$/^{3}EMP1$_\beta$ QP energy shown in Figs. 4(a) and 4(b) is quite similar to that of ^{1}OCC1$_\alpha$/^{1}EMP1$_\alpha$ shown in Fig. 2(l). The main difference is in their spins, i.e., ↑↓ in the triplet excitation case as opposed to ↑↑ in the singlet excitation case. Therefore, we do not encounter any level-crossing in the triplet case in contrast to the singlet case. This results in the dissimilarity between the charge densities of the triplet ^{3}OCC1$_\alpha$ [Fig. 4(h)], ^{3}EMP1$_\beta$ [Fig. 4(j)] levels at 10 fs, the respective ones of the singlet ^{1}OCC1$_\alpha$ [Fig. 2(g)], and the ^{1}EMP1$_\alpha$ [Fig. 2(f)] levels.

At t = 20 fs, the charge isolation around the different fragments becomes more distinct, with OCC2$_\alpha$ clearly representing the isolated H atom's 1*s* character both in charge density [Fig. 4(k)] and in energy [−13.6 eV shown in Fig. 4(a) and Fig. S8(dα) in the supplementary material and in "Triplet excitation" presented in Table II, equal to the exact value of −13.6 eV[76], while OCC1$_\alpha$ [Fig. 4(l) and Fig. S8(eα), and −10.7 eV in "Triplet excitation" presented in Table II], OCC1$_\beta$ [Fig. 4(m) and Fig. S8(cβ), and −13.1 eV in "Triplet excitation" presented in Table II], and EMP1$_\beta$ [Fig. 4(n) and Fig. S8(dβ)] clearly resemble the isolated methyl HOMO$_\alpha$ [Fig. S7(dα) and −11.1 eV in "Triplet excitation" presented in Table II], HOMO$_\beta$ [Fig. S7(cβ) and −13.8 eV in "Triplet excitation" in Table II], and LUMO$_\beta$ [Fig. S7(dβ)] states, respectively. Compared to the LDA energy eigenvalues, the QP energies representing those of the isolated methyl radical levels are in very good agreement with experimentally reported values[75] (presented in the tenth row of Table II).

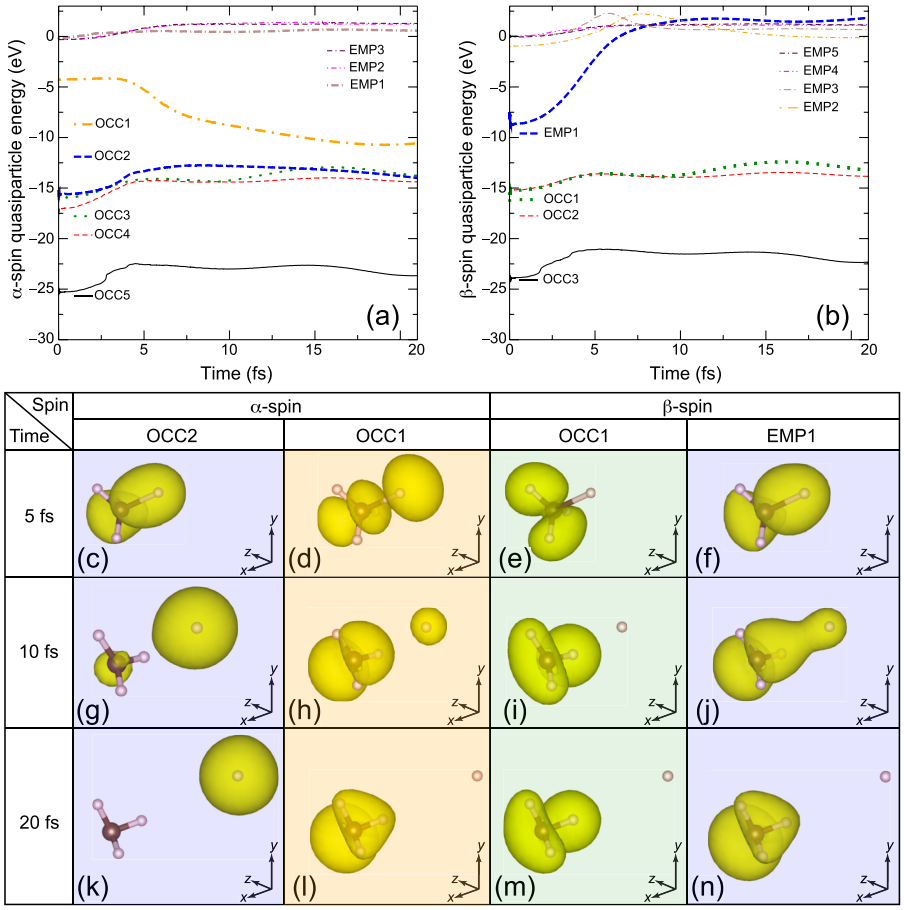

FIG. 4. Temporal change of the QP energies and charge densities for the triplet excitation simulation. Evolution of QP energies of (a) α and (b) β spins with time, obtained from NA-ES-TD*GW*-MD. Panels (c)–(n) indicate the charge densities of $OCC2_\alpha$, $OCC1_\alpha$, $OCC1_\beta$, and $EMP1_\beta$ at $t = 5$ fs [panels (c)–(f)], $t = 10$ fs [panels (g)–(j)], and $t = 20$ fs [panels (k)–(n)]. The colors of each of these panels correspond to the colors of the levels in (a) and (b). The isosurface for the charge density plots was set at 1×10^{-8} electrons/Å^3. The directions of viewing are indicated for reference.

DISCUSSION

The QP energies at $t = 0$ presented in Table I are in very good agreement with those obtained using the relations $\varepsilon_{OCC1} = PAE - IP$ and $\varepsilon_{EMP1} = -PAE - EA$, respectively (values in parentheses) and the experimental values. PAE, ε_{OCC1}, and ε_{EMP1} are expressed in terms of total energies as

$$PAE = E^{(N)}_{HOMO\to LUMO} - E^{(N)}_{GS},$$
$$\varepsilon_{OCC1} = E^{(N)}_{HOMO\to LUMO} - E^{(N-1)}_{HOMO\to vac},$$

and

$$\varepsilon_{EMP1} = E^{(N+1)}_{vac\to LUMO} - E^{(N)}_{HOMO\to LUMO}. \quad (24)$$

Such relations hold not only for the frontier levels but also for all levels in EQPT. Furthermore, Table II presents that the QP energies after the H ejection coincide with those of one-shot *GW* calculations and with the experimentally reported values of the corresponding isolated fragments, which indicates that an accurate description of this photolysis is obtained via NA-ES-TD*GW*-MD.

The power of combining *GW* with EQPT is realized in the fact that one can obtain information of many excited states at the same time without the need for performing individual calculations to track different excited states as is the case, when using wavefunction-theory-based methods, such as CASSCF. The computational cost required for one CASSCF calculation increases factorially with the active space,[77] which is much more demanding than $\mathcal{O}(N_B^4)$ for a *GW* calculation (N_B: number of basis functions). Lack of appropriate treatment of dynamical correlation in traditional CASSCF[77] severely underestimates the vertical excitation energies.[57]

Next, we comment on the quality of our NA-ES-TD*GW*-MD simulations in terms of energy conservation with time. As our formulation of NA-ES-TD*GW*-MD is based primarily on the Ehrenfest framework, we expect the total system energy, which is the sum of the nuclear kinetic energy and total electronic energy, to be invariant with time [see Eq. (24) in Ref. 78]. In the case of TDDFT-MD, the Kohn–Sham eigenvalues do not have a physical meaning and are unreliable. Therefore, the total electronic energy is used along with the nuclear kinetic energy to evaluate the dynamics. On the other

hand, dynamics with quantum chemistry wavefunction-based methods inevitably compute the total energy of electronic states, which are used for monitoring the dynamics. However, in our NA-ESTD*GW*-MD implementation, this information is not necessary to be computed in TD*GW* unlike in the aforementioned methods, as the most important quantity in TD*GW* are the differences between the *GW* total energies of the N electron reference and $(N \pm 1)$ electron ionic systems {referred to as QP energies [Eqs. (1) and (2)]}, which are necessary and sufficient to monitor the dynamics. The reason for not computing the *GW* total energy at every time step is that there is no explicit formulation proposed so far for computing the total electronic energy using the one-shot *GW* approximation. Even if there is some approximate form, its calculation can take additional time and one may lose the advantage of comparable computational cost as TDDFT-MD. In our simulations, we use the information of the total electronic energy only to compute the forces to update the atomic coordinates. This total electronic energy is computed at the LDA level [$E^{(N)}_{\mathrm{LDA}}(\mathbf{R}(t), t)$ in Eq. (20)]; however, it includes some effect of the *GW* correlation through the QP Hamiltonian $\hat{\mathscr{H}}^{\mathrm{QP}}_{\mathrm{mixed}}(\mathbf{R}(t))$. This is not a reflection of the true total electronic energy as both the Fock exchange and the correlation parts of the self-energy are not included. However, the change in the LDA total energy is expected to be almost similar to the true *GW* total energy when the atomic

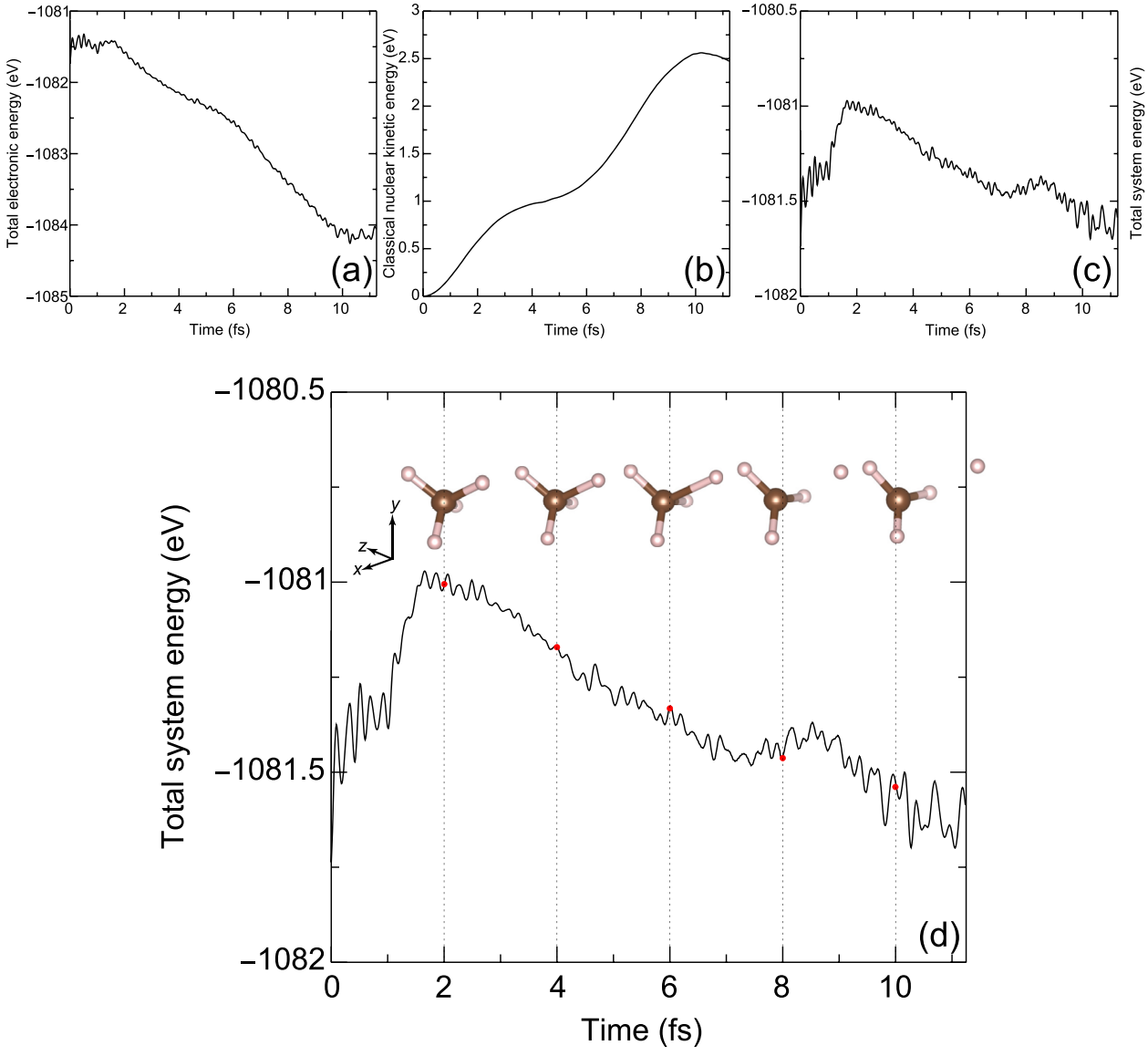

FIG. 5. Conservation of the total energy with time. Temporal change of (a) $E^{(N)}_{\mathrm{LDA}}(\mathbf{R}(t), t)$, (b) classical nuclear kinetic energy, and (c) total system energy [(a) + (b)]. (d) The expanded view of the total system energy with time includes the structures of methane at different time instances. The direction of viewing is indicated for reference.

displacement is very small, rendering the validity to use the LDA total energy to compute the forces [Eq. (20)].

We present the temporal variation of (a) $E^{(N)}_{\mathrm{LDA}}(\mathbf{R}(t),t)$ (labeled as "total electronic energy" in the y-axis), (b) the classical nuclear kinetic energy, and (c) the total system energy [(a) + (b)] for the singlet excitation case (the trend is nearly the same for the other cases) before the surface hopping shown in Fig. 5. As shown in the plots, panel (a) decreases overall by ~2.5 eV, while panel (b) increases by nearly the same amount. Therefore, the total system energy (c) is nearly conserved with a variation within 0.5 eV. This is because during this time interval, the changes in the atomic coordinates [shown through the structures in the expanded total system energy plot in Fig. 5(d)] and the electronic structure are not significant. Hence, the change in $E^{(N)}_{\mathrm{LDA}}(\mathbf{R}(t),t)$ is expected to be nearly similar to that of the true GW total energy.

In the singlet excitation case, the energies of both $\mathrm{OCC1}_\alpha$ and $\mathrm{EMP1}_\alpha$ at the crossing point (at t = 7 fs) are −3.9 eV showing that the zero gap condition [Eq. (3)] is satisfied exactly. This was further verified by computing the total energies of the cationic, anionic, and photoexcited states at the crossing point geometry and inserting them in Eq. (3), which confirmed this condition to within an accuracy of 0.04 eV. This provides clear evidence that EQPT also holds at the crossing point at t = 7 fs. In the spin-preserved and spin-flip channels, $\mathrm{OCC1}_\alpha$, which is occupied by the photoexcited electron, becomes the isolated H level (around −13.2 eV and −13.6 eV, respectively), as expected. In the spin-swap channel, $\mathrm{OCC1}_\alpha$ would eventually become the HOMO_α level of the methyl radical, while $\mathrm{OCC1}_\beta$ becomes the isolated H level. For triplet excitation, one of the deeper, originally occupied threefold degenerate levels, $\mathrm{OCC2}_\alpha$, eventually becomes the isolated hydrogen level around −13.6 eV because there is no other occupied level above $\mathrm{OCC1}_\alpha$. In all the cases, the empty counterpart levels of the H fragment are all located around the vacuum level at $t \geq 20$ fs.

To conclude, we developed a new dynamics methodology, NA-ES-TDGW-MD, based on EQPT to overcome the inapplicability of ALDA to ESs. We successfully applied this method to methane photolysis and demonstrated its remarkable ability of describing the dynamics accurately. Overall, all the QP levels were well described with accurate energies during the simulation with visible charge density distributions, which is only possible by using NA-ES-TDGW-MD. Replacing Kohn–Sham orbitals/energies with *correlated, interacting* quasiparticle orbitals/energies allows the full correspondence to the excited-state surfaces and corresponding total energies, with extended Koopmans' theorem being satisfied. There is no more a need to use a questionable method, such as TDDFT-MD, relying on ALDA.

NA-ES-TDGW-MD tracks all the QP levels simultaneously. In addition, in our TDGW scheme, GW is executed only at the last sub-loop, i.e., in the N_{loops} = 20th sub-loop. GW is known to scale as $\sim \mathcal{O}(N_{\mathrm{B}}^4)$, while DFT with LDA in the remaining $N_{\mathrm{loops}} - 1$ sub-loops scales as $\sim \mathcal{O}(N_{\mathrm{B}}^3)$. Therefore, taking their weighted average gives the cost of our TDGW approach as $\sim \mathcal{O}(N_{\mathrm{B}}^{3-4})$. Both these features indicate that TDGW is distinctly advantageous to dynamics performed with configuration interaction and coupled cluster methods. Thanks to its computational affordability, we are currently using NA-ES-TDGW-MD to investigate the methane photolysis in the presence of transition metal atoms, water photolysis, and proton transfer in DNA molecules, which will appear elsewhere. With more impetus on the study of ultrafast dynamics in nature, NA-ES-TDGW-MD is expected to become the first method of choice to understand the dynamics more intricately before designing experiments that make use of expensive femtosecond laser techniques for the same, thereby redefining the paradigm in the dynamics.

SUPPLEMENTARY MATERIAL

The supplementary material includes the additional results presented in this work.

ACKNOWLEDGMENTS

The calculations in this study were performed using the Numerical Materials Simulator at the National Institute for Materials Science (NIMS); the MASAMUNE supercomputing system at the Center for Computational Materials Science, Institute for Materials Research (IMR), Tohoku University (Proposal No. 19S0501, 20S0505, 202308-SCKGE-0216, and 202212-SCKXX-0506); and the ITO supercomputing system at Kyushu University under the HPCI system project (Project IDs: hp190014, hp190059, hp200040, hp210019, and hp220017) and the JHPCN system project (Project IDs: jh210045 and jh220037). R.S. was supported by the Japan Society for the Promotion of Science (JSPS) KAKENHI (Grant No. 21H01607). K.O. acknowledges the support from the Grant-in-Aid (KAKENHI) for Scientific Research (B) (Grant No. 21H01877) by JSPS. Y.K. was supported by (i) the National Science, Research, and Innovation Fund (NSRF) (NRIIS Project No. 90465); (ii) Thailand Science Research and Innovation (TSRI); and (iii) Suranaree University of Technology (SUT) and was partially supported by the Asian Office of Aerospace Research and Development (Project No. of FA2386-21-1-4024).

AUTHOR DECLARATIONS

Conflict of Interest

The authors have no conflicts to disclose.

Author Contributions

All the authors were involved in designing the research. A.M. and K.O. formulated and implemented NA-ES-TDGW-MD in TOMBO. A.M. performed all the calculations. All the authors contributed to writing the paper.

Aaditya Manjanath: Conceptualization (equal); Data curation (lead); Formal analysis (lead); Investigation (lead); Methodology (equal); Software (equal); Validation (equal); Visualization (lead); Writing – original draft (lead); Writing – review & editing (equal). **Ryoji Sahara**: Conceptualization (equal); Funding acquisition (equal); Project administration (equal); Resources (lead); Supervision (lead); Writing – original draft (supporting); Writing – review & editing (supporting). **Kaoru Ohno**: Conceptualization (equal); Formal analysis (supporting); Funding acquisition

(equal); Investigation (equal); Methodology (equal); Project administration (equal); Software (equal); Supervision (supporting); Validation (equal); Writing – original draft (supporting); Writing – review & editing (equal). **Yoshiyuki Kawazoe**: Conceptualization (equal); Funding acquisition (equal); Project administration (equal); Resources (equal); Supervision (equal); Writing – original draft (supporting); Writing – review & editing (supporting).

DATA AVAILABILITY

The data that support the findings of this study are available within the article, its Supplementary Information, and its supplementary files, `Singlet_excitation_spin-preserved_MD.xyz` and `Triplet_excitation_MD.xyz`. The `xyz` files can be visualized using the VMD software package.[82]

The TOMBO executable used for performing NA-ES-TD*GW*-MD simulations and one-shot *GW* calculations is available upon request.

APPENDIX A: EHRENFEST DYNAMICS

This section demonstrates how the total time-dependent Schrödinger (TDS) equation is factorized exactly into the time-dependent electronic and nuclear component equations and how the Ehrenfest approach for studying the dynamics is formulated by assuming classical nuclear degrees of freedom. The TDS equation for the total wavefunction $\Phi(\{\mathbf{r}_i\},\{\mathbf{R}_I\},t)$ (i and I are electron and nuclear indices, respectively) reads

$$\mathrm{i}\frac{\partial}{\partial t}\Phi(\{\mathbf{r}_i\},\{\mathbf{R}_I\},t) = \mathscr{H}_{\text{total}}(\{\mathbf{r}_i\},\{\mathbf{R}_I\})\Phi(\{\mathbf{r}_i\},\{\mathbf{R}_I\},t) \tag{A1}$$

where $\mathscr{H}_{\text{total}}(\{\mathbf{r}_i\},\{\mathbf{R}_I\})$ is the total Hamiltonian,

$$\begin{aligned}\mathscr{H}_{\text{total}}(\{\mathbf{r}_i\},\{\mathbf{R}_I\}) &= -\sum_I \frac{1}{2M_I}\nabla^2_{\mathbf{R}_I} - \sum_i \frac{1}{2}\nabla^2_{\mathbf{r}_i} + V(\{\mathbf{r}_i\},\{\mathbf{R}_I\}) \\ &= -\sum_I \frac{1}{2M_I}\nabla^2_{\mathbf{R}_I} + \mathscr{H}_{\text{MB}}(\{\mathbf{r}_i\},\{\mathbf{R}_I\})\end{aligned} \tag{A2}$$

with $\mathscr{H}_{\text{MB}}(\{\mathbf{r}_i\},\{\mathbf{R}_I\})$, M_I, and $V(\{\mathbf{r}_i\},\{\mathbf{R}_I\})$ being the many-body (MB) electronic Hamiltonian, the atomic mass of the Ith nucleus, and the total potential containing all the interparticle interactions, respectively. Abedi *et al.* showed that Eq. (A1) can be solved by exactly factorizing $\Phi(\mathbf{r},\mathbf{R},t)$ as[79]

$$\Phi(\{\mathbf{r}_i\},\{\mathbf{R}_I\},t) = \chi(\{\mathbf{R}_I\},t)\Psi(\{\mathbf{r}_i\},\{\mathbf{R}_I\},t), \tag{A3}$$

where $\chi(\{\mathbf{R}_I\},t)$ and $\Psi(\{\mathbf{r}_i\},\{\mathbf{R}_I\},t)$ are the nuclear and electron wavefunctions, respectively. Substituting for $\Phi(\{\mathbf{r}_i\},\{\mathbf{R}_I\},t)$ in Eq. (A1) with its factorized form [Eq. (A3)] gives us the TDS equations for both nuclei and electrons, which are coupled with each other [see Eqs. (6)–(10) in Ref. 79]. Assuming the nuclear density $|\chi(\{\mathbf{R}_I\},t)|^2$ to be a product of delta-functions centered at the atomic positions at time t as

$$|\chi(\{\mathbf{R}_I\},t)|^2 = \prod_I \delta(\mathbf{R}_I - \mathbf{R}_I(t)), \tag{A4}$$

i.e., the localization of the nuclear wavefunction, renders nuclei to be treated as classical particles. With such an assumption (along with the assumption that $\mathscr{H}_{\text{MB}}$ does not change significantly with time), we obtain a form of the electronic TDS equation,

$$\begin{aligned}\mathrm{i}\frac{\partial}{\partial t}\Psi(\{\mathbf{r}_i\};\{\mathbf{R}_I(t)\},t) = [\mathscr{H}_{\text{MB}}(\{\mathbf{r}_i\};\{\mathbf{R}_I(t)\}) \\ - E_{\text{el}}(\{\mathbf{R}_I(t)\},t)]\,\Psi(\{\mathbf{r}_i\};\{\mathbf{R}_I(t)\},t)\end{aligned} \tag{A5}$$

with $E_{\text{el}}(\{\mathbf{R}_I(t)\},t))$ being the total electronic energy (also referred to as the *scalar potential*),

$$\begin{aligned}&E_{\text{el}}(\{\mathbf{R}_I(t)\},t)) \\ &\quad= \left\langle \Psi(\{\mathbf{R}_I(t)\},t)\,\middle|\,\left(\hat{\mathscr{H}}_{\text{MB}}(\{\mathbf{R}_I(t)\}) - \mathrm{i}\frac{\partial}{\partial t}\right)\middle|\,\Psi(\{\mathbf{R}_I(t)\},t)\right\rangle.\end{aligned} \tag{A6}$$

We transform $\Psi(\{\mathbf{r}_i\};\{\mathbf{R}_I(t)\},t)$ such that the $\langle\Psi(\{\mathbf{R}_I(t)\},t)\,|\,\mathrm{i}\frac{\partial}{\partial t}\,|\,\Psi(\{\mathbf{R}_I(t)\},t)\rangle$ term in Eq. (A6) is set to 0.[79] This gives us a new form of the electronic wavefunction,

$$\begin{aligned}\widetilde{\Psi}(\{\mathbf{r}_i\};\{\mathbf{R}_I(t)\},t) = \exp\left(-\mathrm{i}\int_{t_0}^{t} E_{\text{el}}(\{\mathbf{R}_I(t)\},t')\,\mathrm{d}t'\right) \\ \times\,\Psi(\{\mathbf{r}_i\};\{\mathbf{R}_I(t)\},t),\end{aligned} \tag{A7}$$

which, in turn, leads to the standard form of the electronic TDS equation,

$$\mathrm{i}\frac{\partial}{\partial t}\widetilde{\Psi}(\{\mathbf{r}_i\};\{\mathbf{R}_I(t)\},t) = \mathscr{H}_{\text{MB}}(\{\mathbf{r}_i\};\{\mathbf{R}_I(t)\})\,\widetilde{\Psi}(\{\mathbf{r}_i\};\{\mathbf{R}_I(t)\},t). \tag{A8}$$

We note that there is now a parametric dependence of both the time-dependent electronic wavefunction and the MB Hamiltonian on the classical coordinates $\{\mathbf{R}_I(t)\}$. As nuclei now follow classical trajectories, their motion is obtained by invoking the Ehrenfest theorem,

$$\begin{aligned}M_I\frac{\mathrm{d}^2\mathbf{R}_I(t)}{\mathrm{d}t^2} &= -\nabla_{\mathbf{R}_I}\left\langle\widetilde{\Psi}(\{\mathbf{R}_I(t)\},t)\,\middle|\,\hat{\mathscr{H}}_{\text{MB}}(\{\mathbf{R}_I(t)\})\,\middle|\,\widetilde{\Psi}(\{\mathbf{R}_I(t)\},t)\right\rangle \\ &= -\nabla_{\mathbf{R}_I}E_{\text{el}}(\{\mathbf{R}_I(t)\},t).\end{aligned} \tag{A9}$$

The mixed quantum–classical dynamics approach where the electrons are treated quantum mechanically, while the nuclei follow the principles of classical mechanics, is known as the Ehrenfest dynamics. The electronic TDS Eq. (A8) and Newton's Eq. (A9) become the basis of our Ehrenfest dynamics approach. Here, non-adiabatic effects are treated via the surface hopping strategy,[31,60] which is very similar to the *ab initio* multiple cloning technique developed by Makhov *et al.*[36]

APPENDIX B: A SIMPLE DERIVATION OF THE EXTENDED QUASIPARTICLE THEORY (EQPT)

In this section, we demonstrate mathematically how one can obtain the time-dependent quasiparticle equation [Eq. (4)] from the many-body time-dependent electronic Schrödinger equation for any initial (ground/excited) eigenstate of the many-body Hamiltonian and how the QP energies are related to these arbitrary (ground/excited) eigenstates as the initial states as defined in Eqs. (1) and (2). We start by first defining the stationary QP wavefunctions or *overlap amplitudes* (ignoring the necessary spin coordinates for brevity) as

$$\begin{cases} \varphi_i^{\mathrm{QP}}(\mathbf{r};\mathbf{R}(t),t) = \left\langle \Psi_{i\to\mathrm{vac}}^{(N-1)}(\mathbf{R}(t),t) \middle| \hat{\psi}(\mathbf{r}) \middle| \Psi_{\mathrm{ref}}^{(N)}(\mathbf{R}(t),t) \right\rangle, & \text{for occupied } i, \\ \varphi_a^{\mathrm{QP}}(\mathbf{r};\mathbf{R}(t),t) = \left\langle \Psi_{\mathrm{ref}}^{(N)}(\mathbf{R}(t),t) \middle| \hat{\psi}(\mathbf{r}) \middle| \Psi_{\mathrm{vac}\to a}^{(N+1)}(\mathbf{R}(t),t) \right\rangle, & \text{for empty } a, \end{cases} \tag{B1}$$

where $\left|\Psi_{\mathrm{ref}}^{(N)}(\mathbf{R}(t),t)\right\rangle$, $\left|\Psi_{i\to\mathrm{vac}}^{(N-1)}(\mathbf{R}(t),t)\right\rangle$, and $\left|\Psi_{\mathrm{vac}\to a}^{(N+1)}(\mathbf{R}(t),t)\right\rangle$ denote, the initial N-electron reference stationary state and the final $(N\mp1)$-electron stationary states, respectively, $\mathbf{R}(t)\equiv\{\mathbf{R}_I(t)\}$ are the nuclear coordinates with I denoting the atomic index, and $\hat{\psi}(\mathbf{r})$ is the annihilation operator. Since they are the eigenstates of the many-body (MB) electronic Hamiltonian $\hat{\mathscr{H}}_{\mathrm{MB}}(\mathbf{R}(t))$, they satisfy the electronic TDS equations (in atomic units, a.u.),

$$\begin{aligned} \mathrm{i}\frac{\partial}{\partial t}\left|\Psi_\beta^{(M)}(\mathbf{R}(t),t)\right\rangle &= \hat{\mathscr{H}}_{\mathrm{MB}}(\mathbf{R}(t))\left|\Psi_\beta^{(M)}(\mathbf{R}(t),t)\right\rangle \\ &= E_\beta^{(M)}\left|\Psi_\beta^{(M)}(\mathbf{R}(t),t)\right\rangle, \end{aligned} \tag{B2}$$

where $M=N$ or $N\pm1$; $\beta=$ ref, $i\to$ vac, or vac $\to a$ and $\hat{\mathscr{H}}_{\mathrm{MB}}(\mathbf{R}(t))$ is (in the second-quantized form)

$$\begin{aligned} \hat{\mathscr{H}}_{\mathrm{MB}}(\mathbf{R}(t)) = &\int \hat{\psi}^\dagger(\mathbf{r})\left(-\frac{1}{2}\nabla_{\mathbf{r}}^2 + v(\mathbf{r},\mathbf{R}(t))\right)\hat{\psi}(\mathbf{r})\,\mathrm{d}\mathbf{r} \\ &+ \frac{1}{2}\int \hat{\psi}^\dagger(\mathbf{r})\,\hat{\psi}^\dagger(\mathbf{r}')\,\frac{1}{|\mathbf{r}-\mathbf{r}'|}\,\hat{\psi}(\mathbf{r}')\,\hat{\psi}(\mathbf{r})\,\mathrm{d}\mathbf{r}\,\mathrm{d}\mathbf{r}' \\ &+ \sum_{I<J}\frac{Z_I Z_J}{|\mathbf{R}_I(t)-\mathbf{R}_J(t)|}, \end{aligned} \tag{B3}$$

where $v(\mathbf{r},\mathbf{R}(t))$ is the external potential describing the Coulomb interaction between the electrons and nuclei and Z_I is the nuclear charge of the Ith atom. By operating $\mathrm{i}\partial/\partial t$ on Eq. (B1) and using Eq. (B2), it is easy to see that the stationary QP wavefunctions satisfy the TDQP equations,[58,80]

$$\begin{aligned} \mathrm{i}\frac{\partial}{\partial t}\varphi_i^{\mathrm{QP}}(\mathbf{r};\mathbf{R}(t),t) &= \left\langle \Psi_{i\to\mathrm{vac}}^{(N-1)}(\mathbf{R}(t),t)\middle|\left[\hat{\psi}(\mathbf{r}),\hat{\mathscr{H}}_{\mathrm{MB}}(\mathbf{R}(t))\right]\middle|\Psi_{\mathrm{ref}}^{(N)}(\mathbf{R}(t),t)\right\rangle \\ &= \left[E_{\mathrm{ref}}^{(N)} - E_{i\to\mathrm{vac}}^{(N-1)}\right]\left\langle \Psi_{i\to\mathrm{vac}}^{(N-1)}(\mathbf{R}(t),t)\middle|\hat{\psi}(\mathbf{r})\middle|\Psi_{\mathrm{ref}}^{(N)}(\mathbf{R}(t),t)\right\rangle \\ &= \varepsilon_i^{\mathrm{QP}}\varphi_i^{\mathrm{QP}}(\mathbf{r};\mathbf{R}(t),t), \ \text{occupied} \end{aligned} \tag{B4}$$

and

$$\begin{aligned} \mathrm{i}\frac{\partial}{\partial t}\varphi_a^{\mathrm{QP}}(\mathbf{r};\mathbf{R}(t),t) &= \left\langle \Psi_{\mathrm{ref}}^{(N)}(\mathbf{R}(t),t)\middle|\left[\hat{\psi}(\mathbf{r}),\hat{\mathscr{H}}_{\mathrm{MB}}(\mathbf{R}(t))\right]\middle|\Psi_{\mathrm{vac}\to a}^{(N+1)}(\mathbf{R}(t),t)\right\rangle \\ &= \left[E_{\mathrm{vac}\to a}^{(N+1)} - E_{\mathrm{ref}}^{(N)}\right]\left\langle \Psi_{\mathrm{ref}}^{(N)}(\mathbf{R}(t),t)\middle|\hat{\psi}(\mathbf{r})\middle|\Psi_{\mathrm{vac}\to a}^{(N+1)}(\mathbf{R}(t),t)\right\rangle \\ &= \varepsilon_a^{\mathrm{QP}}\varphi_a^{\mathrm{QP}}(\mathbf{r};\mathbf{R}(t),t), \ \text{unoccupied}. \end{aligned} \tag{B5}$$

Using the commutation relation,

$$\begin{aligned} \left[\hat{\psi}(\mathbf{r}),\hat{\mathscr{H}}_{\mathrm{MB}}(\mathbf{R}(t))\right] = &\left(-\frac{1}{2}\nabla_{\mathbf{r}}^2 + v(\mathbf{r},\mathbf{R}(t))\right)\hat{\psi}(\mathbf{r}) \\ &+ \int\frac{1}{|\mathbf{r}-\mathbf{r}'|}\,\hat{\psi}^\dagger(\mathbf{r}')\,\hat{\psi}(\mathbf{r}')\,\hat{\psi}(\mathbf{r})\,\mathrm{d}\mathbf{r}' \end{aligned} \tag{B6}$$

in Eqs. (B4) and (B5), we obtain

$$\begin{aligned} &\left\langle \Psi_{i\to\mathrm{vac}}^{(N-1)}(\mathbf{R}(t),t)\middle|\left[\hat{\psi}(\mathbf{r}),\hat{\mathscr{H}}_{\mathrm{MB}}(\mathbf{R}(t))\right]\middle|\Psi_{\mathrm{ref}}^{(N)}(\mathbf{R}(t),t)\right\rangle \\ &\quad= \left(-\frac{1}{2}\nabla_{\mathbf{r}}^2 + v(\mathbf{r},\mathbf{R}(t))\right)\left\langle \Psi_{i\to\mathrm{vac}}^{(N-1)}(\mathbf{R}(t),t)\middle|\hat{\psi}(\mathbf{r})\middle|\Psi_{\mathrm{ref}}^{(N)}(\mathbf{R}(t),t)\right\rangle \\ &\qquad+ \int\frac{1}{|\mathbf{r}-\mathbf{r}'|}\left\langle \Psi_{i\to\mathrm{vac}}^{(N-1)}(\mathbf{R}(t),t)\middle|\hat{\psi}^\dagger(\mathbf{r}')\,\hat{\psi}(\mathbf{r}')\,\hat{\psi}(\mathbf{r})\middle|\Psi_{\mathrm{ref}}^{(N)}(\mathbf{R}(t),t)\right\rangle\mathrm{d}\mathbf{r}' \\ &\quad= \left(-\frac{1}{2}\nabla_{\mathbf{r}}^2 + v(\mathbf{r},\mathbf{R}(t))\right)\left\langle \Psi_{i\to\mathrm{vac}}^{(N-1)}(\mathbf{R}(t),t)\middle|\hat{\psi}(\mathbf{r})\middle|\Psi_{\mathrm{ref}}^{(N)}(\mathbf{R}(t),t)\right\rangle \\ &\qquad+ \int\Sigma(\mathbf{r},\mathbf{r}';t-t')\left\langle \Psi_{i\to\mathrm{vac}}^{(N-1)}(\mathbf{R}(t),t')\middle|\hat{\psi}(\mathbf{r}')\middle|\Psi_{\mathrm{ref}}^{(N)}(\mathbf{R}(t),t')\right\rangle\mathrm{d}\mathbf{r}'\,\mathrm{d}t', \quad \text{occupied} \end{aligned} \tag{B7}$$

and

$$\begin{aligned}
&\left\langle \Psi_{\mathrm{ref}}^{(N)}(\mathbf{R}(t),t)\left|\left[\hat{\psi}(\mathbf{r}),\hat{\mathscr{H}}_{\mathrm{MB}}(\mathbf{R}(t))\right]\right|\Psi_{\mathrm{vac}\to a}^{(N+1)}(\mathbf{R}(t),t)\right\rangle \\
&\quad=\left(-\frac{1}{2}\nabla_{\mathbf{r}}^2+v(\mathbf{r},\mathbf{R}(t))\right)\left\langle \Psi_{\mathrm{ref}}^{(N)}(\mathbf{R}(t),t)\left|\hat{\psi}(\mathbf{r})\right|\Psi_{\mathrm{vac}\to a}^{(N+1)}(\mathbf{R}(t),t)\right\rangle \\
&\qquad+\int\frac{1}{|\mathbf{r}-\mathbf{r}'|}\left\langle \Psi_{\mathrm{ref}}^{(N)}(\mathbf{R}(t),t)\left|\hat{\psi}^{\dagger}(\mathbf{r}')\,\hat{\psi}(\mathbf{r}')\,\hat{\psi}(\mathbf{r})\right|\Psi_{\mathrm{vac}\to a}^{(N+1)}(\mathbf{R}(t),t)\right\rangle \mathrm{d}\mathbf{r}' \\
&\quad=\left(-\frac{1}{2}\nabla_{\mathbf{r}}^2+v(\mathbf{r},\mathbf{R}(t))\right)\left\langle \Psi_{\mathrm{ref}}^{(N)}(\mathbf{R}(t),t)\left|\hat{\psi}(\mathbf{r})\right|\Psi_{\mathrm{vac}\to a}^{(N+1)}(\mathbf{R}(t),t)\right\rangle \\
&\qquad+\int\Sigma(\mathbf{r},\mathbf{r}';t-t')\left\langle \Psi_{\mathrm{ref}}^{(N)}(\mathbf{R}(t),t')\left|\hat{\psi}(\mathbf{r}')\right|\Psi_{\mathrm{vac}\to a}^{(N+1)}(\mathbf{R}(t),t')\right\rangle \mathrm{d}\mathbf{r}'\,\mathrm{d}t',\quad\text{unoccupied.}
\end{aligned}\tag{B8}$$

Using Eq. (B1), we obtain concise forms of Eqs. (B7) and (B8) as follows:

$$\begin{aligned}
&\left\langle \Psi_{i\to\mathrm{vac}}^{(N-1)}(\mathbf{R}(t),t)\left|\left[\hat{\psi}(\mathbf{r}),\hat{\mathscr{H}}_{\mathrm{MB}}(\mathbf{R}(t))\right]\right|\Psi_{\mathrm{ref}}^{(N)}(\mathbf{R}(t),t)\right\rangle \\
&\quad=\left(-\frac{1}{2}\nabla_{\mathbf{r}}^2+v(\mathbf{r},\mathbf{R}(t))\right)\varphi_i(\mathbf{r};\mathbf{R}(t),t)+\int\Sigma(\mathbf{r},\mathbf{r}';t-t') \\
&\qquad\times\varphi_i(\mathbf{r}';\mathbf{R}(t),t')\,\mathrm{d}\mathbf{r}'\,\mathrm{d}t',\quad\text{occupied,} \\
&\left\langle \Psi_{\mathrm{ref}}^{(N)}(\mathbf{R}(t),t)\left|\left[\hat{\psi}(\mathbf{r}),\hat{\mathscr{H}}_{\mathrm{MB}}(\mathbf{R}(t))\right]\right|\Psi_{\mathrm{vac}\to a}^{(N+1)}(\mathbf{R}(t),t)\right\rangle \\
&\quad=\left(-\frac{1}{2}\nabla_{\mathbf{r}}^2+v(\mathbf{r},\mathbf{R}(t))\right)\varphi_a(\mathbf{r};\mathbf{R}(t),t)+\int\Sigma(\mathbf{r},\mathbf{r}';t-t') \\
&\qquad\times\varphi_a(\mathbf{r}';\mathbf{R}(t),t')\,\mathrm{d}\mathbf{r}'\,\mathrm{d}t',\quad\text{unoccupied.}
\end{aligned}\tag{B9}$$

The TD self-energy $\Sigma(\mathbf{r},\mathbf{r}';\ t-t')$, which includes all the effects of the electron–electron Coulomb interaction, is the same[22,24] for Eqs. (B7)–(B9). At the same time, one can obtain Eqs. (B4) and (B5) as well as Eqs. (B7) and (B8) interchangeably by changing the indices $N-1 \rightleftarrows N$, $(i\to\mathrm{vac}) \rightleftarrows (\mathrm{ref})$, and $(\mathrm{ref}) \rightleftarrows (\mathrm{vac}\to a)$. Equations (B4) and (B5), together with Eq. (B9) give the TDQP equation. While this TDQP equation was previously derived for the N-electron ground state reference by Hedin,[24] the interchangeability between Eqs. (B4) and (B5) as well as between Eqs. (B7) and (B8) demonstrates that the TDQP equation should hold for any N-electron excited eigenstate reference. Note that the self-energy is calculated by TD-MBPT, which is equivalent to Brillouin–Wigner's perturbation theory as explained in Feynman's set of lectures on statistical mechanics.[81] Since Brillouin–Wigner's perturbation theory is applicable to any of the excited eigenstates, it is obvious that all these formulas can be applicable to any reference excited eigenstate. Based on this inference, we can relate the total energy differences in Eqs. (B4) and (B5) (with "ref" corresponding to any N-electron excited eigenstate of the MB Hamiltonian) to the quasiparticle energies as

$$\varepsilon_i^{\mathrm{QP}}=E_{\mathrm{ref}}^{(N)}-E_{i\to\mathrm{vac}}^{(N-1)},\quad\text{occupied}\tag{B10}$$

and

$$\varepsilon_a^{\mathrm{QP}}=E_{\mathrm{vac}\to a}^{(N+1)}-E_{\mathrm{ref}}^{(N)},\quad\text{unoccupied,}\tag{B11}$$

which are Eqs. (1) and (2) in the Main Text. When the time-dependence of $\mathbf{R}(t)$ in Eqs. (B4) and (B5) is weak, we can define the stationary QP wavefunction as

$$\varphi_\alpha^{\mathrm{QP}}(\mathbf{r};\mathbf{R}(t),t')=\varphi_\alpha^{\mathrm{QP}}(\mathbf{r};\mathbf{R}(t))\,\exp\left(-\mathrm{i}\varepsilon_\alpha^{\mathrm{QP}}t'\right).\tag{B12}$$

Using this definition and integrating with respect to t' in Eq. (B9), we obtain the TDQP in Eq. (4). The most important advantage of EQPT is that the initial (stationary) state $\left|\Psi_{\mathrm{ref}}^{(N)}(\mathbf{R}(t),t)\right\rangle$ need not necessarily refer to the ground state but it can also be an arbitrary excited eigenstate of the MB Hamiltonian $\hat{\mathscr{H}}_{\mathrm{MB}}(\mathbf{R}(t))$ [see the interchangeability between Eqs. (B7) and (B8) and also Figs. 1(a) and 1(b) with label "ref"].[22,23]

REFERENCES

[1] P. Hohenberg and W. Kohn, "Inhomogeneous electron gas," Phys. Rev. **136**, B864–B871 (1964).
[2] W. Kohn and L. J. Sham, "Self-consistent equations including exchange and correlation effects," Phys. Rev. **140**, A1133–A1138 (1965).
[3] E. Runge and E. K. U. Gross, "Density-functional theory for time-dependent systems," Phys. Rev. Lett. **52**, 997–1000 (1984).
[4] O. Sugino and Y. Miyamoto, "Density-functional approach to electron dynamics: Stable simulation under a self-consistent field," Phys. Rev. B **59**, 2579–2586 (1999).
[5] F. Cordova *et al.*, "Troubleshooting time-dependent density-functional theory for photochemical applications: Oxirane," J. Chem. Phys. **127**, 164111 (2007).
[6] I. Tavernelli, B. F. E. Curchod, and U. Rothlisberger, "Mixed quantum-classical dynamics with time-dependent external fields: A time-dependent density-functional-theory approach," Phys. Rev. A **81**, 052508 (2010).
[7] R. Sahara, H. Mizuseki, M. H. F. Sluiter, K. Ohno, and Y. Kawazoe, "Effect of a nickel dimer on the dissociation dynamics of a hydrogen molecule," RSC Adv. **3**, 12307–12312 (2013).
[8] G. Wachter *et al.*, "*Ab initio* simulation of electrical currents induced by ultrafast laser excitation of dielectric materials," Phys. Rev. Lett. **113**, 087401 (2014).
[9] K. Tsubonoya, C. Hu, and K. Watanabe, "Time-dependent density-functional theory simulation of electron wave-packet scattering with nanoflakes," Phys. Rev. B **90**, 035416 (2014).
[10] E. Irani, A. Anvari, and R. Sadighi-Bonabi, "Selective photo-dissociative ionization of methane molecule with TDDFT study," Spectrochim. Acta, Part A **171**, 325–329 (2017).
[11] E. E. Quashie, B. C. Saha, X. Andrade, and A. A. Correa, "Self-interaction effects on charge-transfer collisions," Phys. Rev. A **95**, 042517 (2017).

[12]Y. Miyamoto and T. Komatsu, "Molecular-scale modeling of light emission by combustion: An *ab initio* study," Sci. Rep. **9**, 12707 (2019).
[13]X. Jiang *et al.*, "Real-time *GW*-BSE investigations on spin-valley exciton dynamics in monolayer transition metal dichalcogenide," Sci. Adv. **7**, eabf3759 (2021).
[14]M. Petersilka, U. J. Gossmann, and E. K. U. Gross, "Excitation energies from time-dependent density-functional theory," Phys. Rev. Lett. **76**, 1212–1215 (1996).
[15]M. M. Morrell, R. G. Parr, and M. Levy, "Calculation of ionization potentials from density matrices and natural functions, and the long-range behavior of natural orbitals and electron density," J. Chem. Phys. **62**, 549–554 (1975).
[16]D. W. Smith and O. W. Day, "Extension of Koopmans' theorem. I. Derivation," J. Chem. Phys. **62**, 113–114 (1975).
[17]J. F. Janak, "Proof that $\frac{\partial e}{\partial n_i} = \varepsilon$ in density-functional theory," Phys. Rev. B **18**, 7165–7168 (1978).
[18]J. Heyd, G. E. Scuseria, and M. Ernzerhof, "Hybrid functionals based on a screened Coulomb potential," J. Chem. Phys. **118**, 8207–8215 (2003).
[19]L. Kronik, T. Stein, S. Refaely-Abramson, and R. Baer, "Excitation gaps of finite-sized systems from optimally tuned range-separated hybrid functionals," J. Chem. Theory Comput. **8**, 1515–1531 (2012).
[20]C. Li, X. Zheng, N. Q. Su, and W. Yang, "Localized orbital scaling correction for systematic elimination of delocalization error in density functional approximations," Natl. Sci. Rev. **5**, 203–215 (2017).
[21]I. Dabo *et al.*, "Koopmans' condition for density-functional theory," Phys. Rev. B **82**, 115121 (2010).
[22]K. Ohno, S. Ono, and T. Isobe, "A simple derivation of the exact quasiparticle theory and its extension to arbitrary initial excited eigenstates," J. Chem. Phys. **146**, 084108 (2017).
[23]K. Ohno, K. Esfarjani, and Y. Kawazoe, *Computational Materials Science: From Ab Initio to Monte Carlo Methods*, 2nd ed. (Springer-Verlag, Heidelberg, 2018).
[24]L. Hedin, "New method for calculating the one-particle green's function with application to the electron-gas problem," Phys. Rev. **139**, A796–A823 (1965).
[25]T. Isobe, R. Kuwahara, and K. Ohno, "*GW*(Γ) method without the Bethe–Salpeter equation for photoabsorption energies of spin-polarized systems," Phys. Rev. A **97**, 060502(R) (2018).
[26]T. Aoki and K. Ohno, "*Ab initio* simulations of x-ray emission spectroscopy with the *GW* + Bethe-Salpeter equation method," Phys. Rev. B **100**, 075149 (2019).
[27]K. Ohno and T. Aoki, "Extended quasiparticle approach to non-resonant and resonant X-ray emission spectroscopy," Phys. Chem. Chem. Phys. **24**, 16586–16595 (2022).
[28]M. S. Hybertsen and S. G. Louie, "First-principles theory of quasiparticles: Calculation of band gaps in semiconductors and insulators," Phys. Rev. Lett. **55**, 1418–1421 (1985).
[29]T. N. Pham, S. Ono, and K. Ohno, "*Ab initio* molecular dynamics simulation study of successive hydrogenation reactions of carbon monoxide producing methanol," J. Chem. Phys. **144**, 144309 (2016).
[30]J. C. Tully and R. K. Preston, "Trajectory surface hopping approach to nonadiabatic molecular collisions: The reaction of H^+ with D_2," J. Chem. Phys. **55**, 562–572 (1971).
[31]J. C. Tully, "Molecular dynamics with electronic transitions," J. Chem. Phys. **93**, 1061–1071 (1990).
[32]T. J. Martinez, M. Ben-Nun, and G. Ashkenazi, "Classical/quantal method for multistate dynamics: A computational study," J. Chem. Phys. **104**, 2847–2856 (1996).
[33]T. J. Martinez, M. Ben-Nun, and R. D. Levine, "Multi-electronic-state molecular dynamics: A wave function approach with applications," J. Phys. Chem. **100**, 7884–7895 (1996).
[34]M. Ben-Nun, J. Quenneville, and T. J. Martínez, "*Ab initio* multiple spawning: Photochemistry from first principles quantum molecular dynamics," J. Phys. Chem. A **104**, 5161–5175 (2000).
[35]B. Mignolet and B. F. E. Curchod, "A walk through the approximations of *ab initio* multiple spawning," J. Chem. Phys. **148**, 134110 (2018).
[36]D. V. Makhov, W. J. Glover, T. J. Martinez, and D. V. Shalashilin, "*Ab initio* multiple cloning algorithm for quantum nonadiabatic molecular dynamics," J. Chem. Phys. **141**, 054110 (2014).
[37]B. F. E. Curchod and T. J. Martínez, "*Ab initio* nonadiabatic quantum molecular dynamics," Chem. Rev. **118**, 3305–3336 (2018).
[38]M. Beck, A. Jäckle, G. Worth, and H.-D. Meyer, "The multiconfiguration time-dependent hartree (MCTDH) method: A highly efficient algorithm for propagating wavepackets," Phys. Rep. **324**, 1–105 (2000).
[39]J. Warnatz, "Rate coefficients in the C/H/O system," in *Combustion Chemistry*, edited by W. C. Gardiner (Springer, New York, 1984), pp. 197–360.
[40]K. Sakaguchi, S. Fukutani, and H. Jinno, "Combustion reaction mechanism in coaxial methane/air diffusion flame," Nippon Kagaku Kaishi **12**, 2037–2044 (1988).
[41]S. Fukutani, K. Sakaguchi, N. Kunioshi, and H. Jinno, "Combustion reactions in methane-air premixed flames," Bull. Chem. Soc. Jpn. **64**, 1623–1631 (1991).
[42]C. K. Westbrook, F. L. Dryer, and K. Schug, "Numerical modeling of ethylene oxidation in laminar flames," Combust. Flame **52**, 299–313 (1983).
[43]M. Yousefi and S. Donne, "Experimental study for thermal methane cracking reaction to generate very pure hydrogen in small or medium scales by using regenerative reactor," Front. Energy Res. **10**, 1–12 (2022).
[44]A. M. Mebel, S.-H. Lin, and C.-H. Chang, "Theoretical study of vibronic spectra and photodissociation pathways of methane," J. Chem. Phys. **106**, 2612–2620 (1997).
[45]R. van Harrevelt, "Photodissociation of methane: Exploring potential energy surfaces," J. Chem. Phys. **125**, 124302 (2006).
[46]P. A. Cook *et al.*, "Vacuum ultraviolet photochemistry of methane, silane and germane," Phys. Chem. Chem. Phys. **3**, 1848–1860 (2001).
[47]J.-H. Wang and K. Liu, "VUV photochemistry of CH_4 and isotopomers. I. Dynamics and dissociation pathway of the H/D-atom elimination channel," J. Chem. Phys. **109**, 7105–7112 (1998).
[48]J.-H. Wang *et al.*, "Vacuum ultraviolet photochemistry of CH_4 and isotopomers. II. Product channel fields and absorption spectra," J. Chem. Phys. **113**, 4146–4152 (2000).
[49]A. J. R. Heck, R. N. Zare, and D. W. Chandler, "Photofragment imaging of methane," J. Chem. Phys. **104**, 4019–4030 (1996).
[50]R. Brownsword *et al.*, "Quantum yield for H atom formation in the methane dissociation after photoexcitation at the lyman-α (121.6 nm) wavelength," Chem. Phys. Lett. **266**, 259–266 (1997).
[51]L. C. Lee and C. C. Chiang, "Fluorescence yield from photodissociation of CH_4 at 1060-1420 Å," J. Chem. Phys. **78**, 688–691 (1983).
[52]A. H. Laufer and J. R. McNesby, "Photolysis of methane at 1236-Å: Quantum yield of hydrogen formation," J. Chem. Phys. **49**, 2272–2278 (1968).
[53]R. Rebbert and P. Ausloos, "Photolysis of methane: Quantum yield of $C(^1D)$ and CH," J. Photochem. **1**, 171–176 (1972).
[54]A. P. York, T. Xiao, and M. L. Green, "Brief overview of the partial oxidation of methane to synthesis gas," Top. Catal. **22**, 345–358 (2003).
[55]Y. Matsumura and T. Nakamori, "Steam reforming of methane over nickel catalysts at low reaction temperature," Appl. Catal., A **258**, 107–114 (2004).
[56]C.-Z. Gao, J. Wang, and F.-S. Zhang, "Collision of H^+ + CH_4 at 30 eV: A simulation study," Nucl. Instrum. Methods Phys. Res., Sect. B **307**, 225–228 (2013).
[57]M. D. Lodriguito, G. Lendvay, and G. C. Schatz, "Trajectory surface-hopping study of methane photodissociation dynamics," J. Chem. Phys. **131**, 224320 (2009).
[58]T. Nakashima, H. Raebiger, and K. Ohno, "Normalization of exact quasiparticle wave functions in the green's function method guaranteed by the ward identity," Phys. Rev. B **104**, L201116 (2021).
[59]U. Saalmann and R. Schmidt, "Non-adiabatic quantum molecular dynamics: Basic formalism and case study," Z. Phys. D Atom. Mol. Cl. **38**, 153–163 (1996).
[60]O. V. Prezhdo and P. J. Rossky, "Mean-field molecular dynamics with surface hopping," J. Chem. Phys. **107**, 825–834 (1997).
[61]M. S. Hybertsen and S. G. Louie, "Electron correlation in semiconductors and insulators: Band gaps and quasiparticle energies," Phys. Rev. B **34**, 5390–5413 (1986).
[62]C. Tully, "Mixed quantum–classical dynamics," Faraday Discuss. **110**, 407–419 (1998).
[63]J. C. Tully, *Nonadiabatic Dynamics* (World Scientific, Singapore, 1998), Chap. 2, pp. 34–72.

[64]K. Ohno *et al.*, "Extensive first-principles molecular dynamics study on Li encapsulation into C_{60} and its experimental confirmation," Nanoscale **10**, 1825–1836 (2018).
[65]T. Ohtsuki *et al.*, "Creation of Mo/Tc@C_{60} and Au@C_{60} and molecular-dynamics simulations," RSC Adv. **11**, 19666–19672 (2021).
[66]S. Ono, Y. Noguchi, R. Sahara, Y. Kawazoe, and K. Ohno, "TOMBO: All-electron mixed-basis approach to condensed matter physics," Comput. Phys. Commun. **189**, 20–30 (2015).
[67]S. Ishii, K. Ohno, Y. Kawazoe, and S. G. Louie, "*Ab initio* GW quasiparticle energies of small sodium clusters by an all-electron mixed-basis approach," Phys. Rev. B **63**, 155104 (2001).
[68]R. Kuwahara, Y. Tadokoro, and K. Ohno, "Validity of virial theorem in all-electron mixed basis density functional, Hartree-Fock, and GW calculations," J. Chem. Phys. **141**, 084108 (2014).
[69]W. H. Press, S. A. Teukolsky, W. T. Vetterling, and B. P. Flannery, *Numerical Recipes in C*, 2nd ed. (Cambridge University Press, Cambridge, USA, 1992).
[70]K. M. Ho, C. Elsasser, C. T. Chan, and M. Fahnle, "First-principles pseudopotential calculations for hydrogen in 4d transition metals. I. Mixed-basis method for total energies and forces," J. Phys. Condens. Matter **4**, 5189 (1992).
[71]R. M. Parrish, E. G. Hohenstein, and T. J. Martínez, "'Balancing the block Davidson-Liu algorithm," J. Chem. Theory Comput. **12**, 3003–3007 (2016).
[72]J. E. Collin and J. Delwiche, "Ionization of methane and its electronic energy levels," Can. J. Chem. **45**, 1875–1882 (1967).
[73]K. Watanabe, "Ionization potentials of some molecules," J. Chem. Phys. **26**, 542–547 (1957).
[74]S. Katagiri and S. Kohda-Sudoh, "Bond orbital calculations on the methane and silane molecules. II. Vertical transition energies of the lower singlet-excited states of CH_4," Bull. Chem. Soc. Jpn. **51**, 1009–1011 (1978).
[75]NIST Electron-Impact Ionization Cross Sections https://physics.nist.gov/cgi-bin/Ionization/table.pl?ionization=CH3.
[76]NIST Chemistry WebBook https://webbook.nist.gov/cgi/cbook.cgi?ID=C12385136&Units=SI&Mask=9A0.
[77]B. Roos, M. Fülscher, P.-Å. Malmqvist, M. Merchán, and L. Serrano-Andrés, *Multiconfigurational SCF Theory* (John Wiley & Sons, Ltd., 2016), Chap. 9, pp. 103–130.
[78]E. V. Arribas, L. M. Ibele, D. Lauvergnat, N. T. Maitra, and F. Agostini, "Significance of energy conservation in coupled-trajectory approaches to nonadiabatic dynamics," J. Chem. Theory Comput. **19**, 7787–7800 (2023).
[79]A. Abedi, N. T. Maitra, and E. K. U. Gross, "Exact factorization of the time-dependent electron-nuclear wave function," Phys. Rev. Lett. **105**, 123002 (2010).
[80]A. Klein and R. Prange, "Perturbation theory for an infinite medium of fermions," Phys. Rev. **112**, 994–1007 (1958).
[81]R. P. Feynman, *Statistical Mechanics: A Set of Lectures*, *Advanced Books Classics* (Chapman and Hall/CRC, 1972).
[82]W. Humphrey, A. Dalke, and K. Schulten, "VMD: Visual molecular dynamics," J. Mol. Graphics **14**, 33–38 (1996).